Cell Reports



# β1 integrin signaling governs necroptosis via the chromatin-remodeling factor CHD4

## Graphical abstract

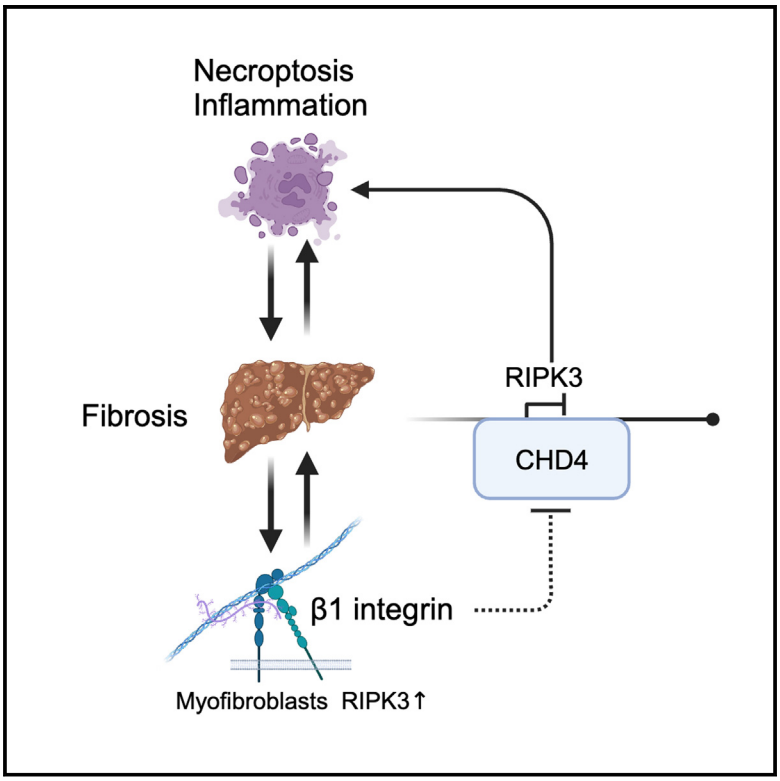


## Authors

Zhiqi Sun, Filippo M. Cernilogar, Helena Horvatic, Assa Yeroslaviz, Zeinab Abdullah, Gunnar Schotta, Veit Hornung

## Correspondence

zsun@genzentrum.lmu.de (Z.S.), hornung@genzentrum.lmu.de (V.H.)

## In brief

Sun et al. identify myofibroblasts as the major cell type expressing RIPK3 in bile-duct-ligation-induced liver fibrosis. Profibrotic β1 integrin signaling functions as the upstream driver of RIPK3 expression in fibroblasts. Loss of β1 integrin leads to CHD4-mediated epigenetic repression of *Ripk3* independent of the NuRD or ChAHP complex.

## Highlights

- Myofibroblasts are the major cell type expressing RIPK3 in induced liver fibrosis
- Loss of profibrotic β1 integrin leads to epigenetic repression of *Ripk3* by CHD4
- CHD4 represses the Ripk3 locus in a NuRD- and ChAHP-independent manner
- The stand-alone function of CHD4 exhibits exquisite locus specificity

Sun et al., 2023, Cell Reports *42*, 113322
November 28, 2023 
https://doi.org/10.1016/j.celrep.2023.113322

Cell Reports

CellPress
OPEN ACCESS

Article

# β1 integrin signaling governs necroptosis via the chromatin-remodeling factor CHD4

Zhiqi Sun,[1,2,*] Filippo M. Cernilogar,[3] Helena Horvatic,[4] Assa Yeroslaviz,[5] Zeinab Abdullah,[4] Gunnar Schotta,[3] and Veit Hornung[1,2,6,*]

[1]Gene Center and Department of Biochemistry, Ludwig Maximilian University of Munich, Munich, Germany
[2]Research Group Molecular Mechanisms of Inflammation, Max-Planck Institute of Biochemistry, Martinsried, Germany
[3]Division of Molecular Biology, Biomedical Center, Faculty of Medicine, Ludwig Maximilian University of Munich, Munich, Germany
[4]Institute of Molecular Medicine and Experimental Immunology, University Hospital Bonn, Bonn, Germany
[5]Computational Biology Group, Max-Planck Institute of Biochemistry, Martinsried, Germany
[6]Lead contact
*Correspondence: zsun@genzentrum.lmu.de (Z.S.), hornung@genzentrum.lmu.de (V.H.)
https://doi.org/10.1016/j.celrep.2023.113322

## SUMMARY

Fibrosis, characterized by sustained activation of myofibroblasts and excessive extracellular matrix (ECM) deposition, is known to be associated with chronic inflammation. Receptor-interacting protein kinase 3 (RIPK3), the central kinase of necroptosis signaling, is upregulated in fibrosis and contributes to tumor necrosis factor (TNF)-mediated inflammation. In bile-duct-ligation-induced liver fibrosis, we found that myofibroblasts are the major cell type expressing RIPK3. Genetic ablation of β1 integrin, the major profibrotic ECM receptor in fibroblasts, not only abolished ECM fibrillogenesis but also blunted RIPK3 expression via a mechanism mediated by the chromatin-remodeling factor chromodomain helicase DNA-binding protein 4 (CHD4). While the function of CHD4 has been conventionally linked to the nucleosome-remodeling deacetylase (NuRD) and CHD4-ADNP-HP1(ChAHP) complexes, we found that CHD4 potently repressed a set of genes, including *Ripk3*, with high locus specificity but independent of either the NuRD or the ChAHP complex. Thus, our data uncover that β1 integrin intrinsically links fibrotic signaling to RIPK3-driven inflammation via a novel mode of action of CHD4.

## INTRODUCTION

Tissue fibrosis is initiated by a prolonged wound-healing response during chronic tissue injury and inflammation. It is characterized by sustained activation of myofibroblasts that mediate excessive deposition of extracellular matrix (ECM), such as collagen and fibronectin, and tissue stiffening.[1] As the major receptors mediating cell adhesion to the ECM, integrins in myofibroblasts play a pivotal role in fibrosis.[2,3] 24 heterodimeric integrin receptors are expressed in vertebrates. Among these, a group of β1-containing integrin receptors bind collagens (α1β1, α2β1, α10β1, α11β1) and fibronectin (α5β1), mediate ECM fibrillogenesis, promote cellular contractility, and instruct a profibrotic gene expression program through the MKL1-SRF and YAP/TAZ transcription factor networks.[4–6] Blocking β1 integrin prevents ECM fibrillogenesis, reduces cellular contractility, and blunts profibrotic gene expression.[5,7] In contrast to β1 integrin, αVβ3 integrin binds fibronectin but not collagen, cannot mediate fibrillogenesis, but can synergize with β1 integrins to promote cellular contractility.[4]

Myofibroblast activation during tissue injury and wound healing is driven by a myriad of profibrotic and proinflammatory cytokines, most notably transforming growth factor β (TGF-β), interleukin-1β (IL-1β), and tumor necrosis factor α (TNF-α). Binding of TNF-α to TNFR1 triggers a membrane-bound receptor signaling complex and receptor-interacting protein kinase 1 (RIPK1)-dependent nuclear factor κB (NF-κB) signaling. Activated RIPK1 can subsequently assemble a cytosolic complex consisting of FAS-associated death domain-containing protein (FADD) and caspase-8, which triggers caspase-8 activation and extrinsic apoptosis.[8] Insufficient caspase-8 activity, however, results in the formation of a large amyloid-like signaling complex via RHIM-motif-mediated oligomerization of RIPK1 and RIPK3.[9–12] Subsequently, activated RIPK3 phosphorylates pseudokinase mixed-lineage kinase domain-like protein (MLKL) on Ser345 and Ser347 for murine MLKL (Thr357 and Ser358 for human MLKL), which releases MLKL autoinhibition and drives its oligomerization at the plasma membrane to induce membrane rupture and a lytic form of cell death known as necroptosis.[13–16] During necroptosis, dying cells unleash damage-associated molecular patterns (DAMPs) and alarmins such as IL-1 family cytokines, as well as TNF-α.[17,18] Furthermore, RIPK3 can cooperate with RIPK1 to promote cytokine expression, thereby instigating a self-amplifying inflammatory signaling loop that impacts on the cell microenvironment beyond cell death.[19,20] Blocking TNF-α signaling alleviates fibrosis in multiple organs including liver, lung, and kidney and in fibrosis associated with Duchenne muscular dystrophy (DMD) and Dupuytren's disease.[21–23]

Interestingly, RIPK3 upregulation correlates with disease progression in large cohort of human patients with non-alcoholic steatohepatitis (NASH).[24] RIPK3 upregulation has also been reported in lung fibrosis,[25] kidney fibrosis,[26] and DMD, which is associated with muscle fibrosis,[23,27] suggesting a universal mechanism driving RIPK3 expression in fibrosis. The cell types that express RIPK3 within fibrotic tissues are controversial. While RIPK3 upregulation has been attributed to fibroblasts in renal fibrosis,[26] RIPK3 remains silenced by promoter methylation in hepatocytes in NASH,[28] suggesting that non-hepatic cells may contribute to RIPK3 upregulation in liver fibrosis. Nevertheless, genetic ablation of RIPK3 alleviates unilateral ureteral-obstruction-induced or adenine-diet-induced renal fibrosis,[26] methionine- and choline-deficient-diet-induced steatohepatitis,[29] and DMD-associated muscle fibrosis.[23]

How RIPK3 expression is regulated in fibrosis remains poorly understood. While the *Ripk3* locus is silenced by DNMT1-mediated promoter methylation in *in-vitro*-cultured cancer cell lines,[30] the CHD4-containing NuRD complex represses RIPK3 expression in endothelial cells and muscle stem cells.[27,31] The NuRD complex is composed of at least 7 subunits, each with at least 2 paralogs, including class II chromodomain helicase DNA-binding (CHD) proteins CHD3/4/5, GATAD2A/B, CDK2AP1/2, MBD2/3, MTA1/2/3, RBBP4/7, and HDAC1/2.[32] By CHD-dependent nucleosome sliding and HDAC1/2-mediated erasure of active transcription marks such as H3K27Ac, NuRD generally functions as a transcriptional repressor. Class II CHDs also form another complex with activity-dependent neuroprotector homeobox (ADNP) and heterochromatin protein 1 (HP1), known as the ChAHP complex.[33,34] Together, NuRD and ChAHP constitute most of the high-affinity interactors of class II CHDs[34,35] and are thought to account for the majority of their functions in stem cell maintenance, cell lineage specification, viral latency, hemoglobin switch, and DNA damage repair.[36–41] On the other hand, CHD4 only peripherally associates with the remainder of the NuRD complex[42,43] and has nucleosome-remodeling activity by itself,[44] suggesting a possible NuRD- and ChAHP-independent function.

Here, we investigated the cell-autonomous regulation between fibrotic signaling and RIPK3-mediated TNF signaling in fibroblasts. We found strong RIPK3 expression in both myofibroblasts and macrophages in liver fibrosis induced by bile duct ligation. Genetic ablation of the profibrotic β1 integrin receptor in fibroblasts not only abolished the fibrotic signature but also reduced RIPK3 expression through CHD4-mediated repression at the proximal enhancer element within the *Ripk3* locus. Surprisingly, despite its high locus specificity, CHD4-mediated repression of RIPK3 operated independently of the NuRD or ChAHP complex, arguing for the existence of additional CHD4-containing complexes that regulate locus-specific gene expression.

## RESULTS

### β1 integrin links fibrotic signaling with RIPK3 expression in fibroblasts

Numerous reports of RIPK3 upregulation in liver fibrosis and the lack of necroptosis in hepatocytes[24,28,29,45] prompted us to define the spatial expression of RIPK3 in a bile duct ligation (BDL)-induced liver fibrosis model. Two RIPK3 antibodies (D4G2A, CST; ab62344, Abcam) robustly detected endogenous RIPK3 in paraformaldehyde (PFA)-fixed mouse MOVAS smooth muscle cells, while the immunofluorescence was dramatically reduced in *Ripk3* knockout (KO) MOVAS cells (Figures S1A and S1B). Whereas RIPK3 was sparsely detected in the healthy liver by the D4G2A antibody, most likely in Kupffer cells, RIPK3 expression was significantly increased in fibrotic liver tissue, mostly within fibrotic scars where smooth muscle actin (SMA)-positive myofibroblasts and infiltrating CD11b-positive myeloid cells were tightly intercalated but also slightly in the surrounding hepatocytes (Figure S1C). While RIPK3 is known to be expressed in macrophages, we observed comparably high RIPK3 expression in myofibroblasts (Figure S1D). Immunostaining with another RIPK3 antibody (ab62344) confirmed that RIPK3 was upregulated in BDL-induced liver fibrosis colocalizing with the mesenchyme marker Vimentin (Figures S1E and S1F). Compared with healthy liver, the mean fluorescence intensity of RIPK3 immunolabeling was increased 3-fold in the fibrotic area, in parallel with Vimentin signals, and moderately increased by 50% in the surrounding area (Figures S1G and S1H).

Myofibroblasts deposit excessive ECM and mediate tissue stiffening through integrin receptors. To test whether fibrotic signaling regulates RIPK3 expression in fibroblasts, we modeled fibrotic and non-fibrotic conditions using a set of well-established integrin pan-KO fibroblast cell lines in which fibrillogenic β1 integrin and non-fibrillogenic αV integrin are reconstituted individually (hereafter referred to as pKO-β1 and pKO-αV, respectively) or in combination (pKO-αV/β1).[4] Immunostaining of a confluent culture of these cells for collagen type 3 confirmed that only pKO-β1 and pKO-αV/β1 cells, but not pKO-αV cells, assembled elaborated collagen-3 ECM fibers (Figure 1A). Intriguingly, combined treatment of TNF-α and pan-caspase inhibitor zVAD triggered massive necroptosis in pKO-β1 cells, as revealed by SytoxGreen labeling, whereas the non-fibrotic pKO-αV cells were completely resistant to necroptosis (Figure 1A). Fibroblasts expressing both αV and β1 integrins showed an intermediate phenotype with moderate necroptosis (Figure 1A). Live-cell imaging with SytoxGreen revealed hypersensitive kinetics of necroptosis in pKO-β1 cells that started 3 h after TNF-α/zVAD treatment (Figure 1B). In contrast, minimal lytic cell death was observed in pKO-αV cells even after a period of 10 h (Figure 1B). A lactate dehydrogenase (LDH) release assay further confirmed the complete lack of necroptosis in pKO-αV cells (Figure 1C). The differential necroptosis response is not caused by altered RIPK1 signaling, as comparable RIPK1-dependent induction of *Cxcl10* and *Cxcl1* mRNAs was observed in the three cell lines (Figure S1I). Instead, the degree of necroptosis correlated with MLKL phosphorylation at Ser345 by RIPK3 (Figure 1D). Interestingly, whereas high and intermediate levels of RIPK3 protein were expressed in pKO-β1 and pKO-αV/β1 cells, respectively, no RIPK3 protein expression could be detected in pKO-αV cells (Figure 1D), suggesting a positive correlation between β1 integrin and RIPK3 expression in these cells. qPCR analysis revealed that while high and intermediate levels of *Ripk3* mRNA were detected in pKO-β1 and pKO-αV/β1 cells, *Ripk3* mRNA expression was markedly repressed in pKO-αV cells (Figure 1E). Strikingly, RNA sequencing (RNA-seq) analysis of the three

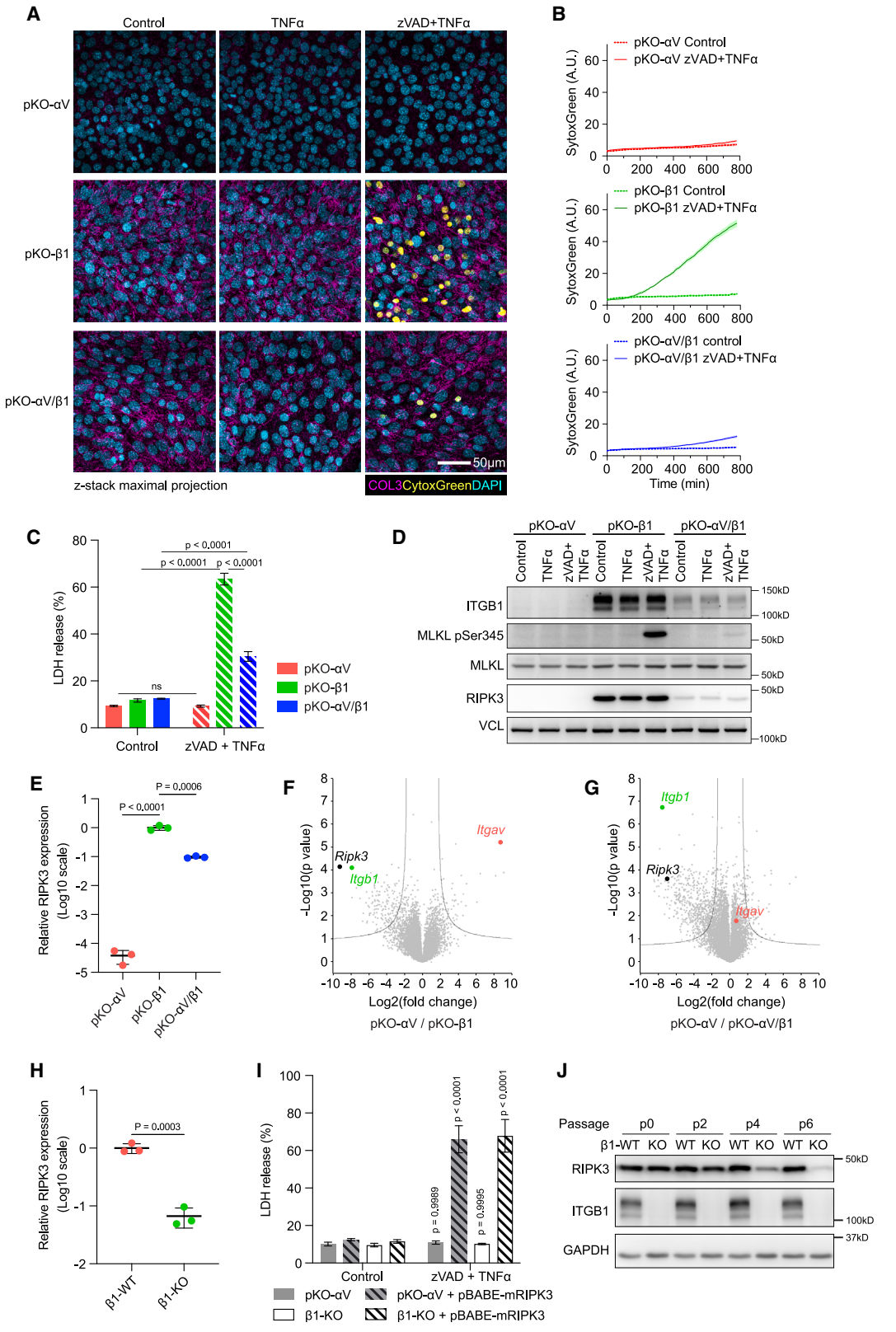


*(legend on next page)*

integrin-reconstituted cell lines revealed that *Ripk3* mRNA was the most significantly upregulated transcript in β1-integrin-expressing cells (Table S3; Figures 1F and 1G).

To further confirm these observations, we used an SV40 large T antigen-immortalized fibroblast cell line derived from β1 integrin floxed mice (hereafter referred to as β1-WT [wild type]).[46] Cre-recombinase-mediated deletion of β1 integrin (β1-KO) led to significant reduction of *Ripk3* mRNA expression (Figure 1H). The reduced RIPK3 protein expression in β1-KO cells was confirmed by western blot (Figure S1J) using monoclonal RIPK3 antibodies against the C terminus (D4G2A) and the N terminus (8G7) of RIPK3.[47,48] Like pKO-αV cells, β1-KO fibroblasts were entirely resistant to TNF-α-induced necroptosis, which could be rescued by lentivirus-mediated reconstitution of RIPK3, indicating that RIPK3 is the only missing component for necroptosis in β1-integrin-deficient cells (Figure 1I). To further understand how β1 integrin deficiency leads to diminished RIPK3 expression, we infected an early passage of β1 integrin floxed fibroblasts with adenovirus expressing Cre recombinase and used fluorescence-activated cell sorting (FACS) to isolate β1-KO cells by surface labeling 2 days after Cre expression. Sorted cells (designated as passage 0 [P0]) were passaged every 2 days thereafter. Whereas RIPK3 expression was maintained after β1 integrin deletion in P0 cells, reduction of RIPK3 became discernible at P2, which was succeeded by progressive loss of RIPK3 in the following passages (Figure 1J). In conclusion, our data indicate that RIPK3 expression, and thus sensitivity to necroptosis-inducing stimuli, is profoundly affected by β1 integrin signaling and suggest a persistent epigenetic mechanism operating behind this phenomenon.

## CHD4, but not DNMT, represses RIPK3 expression in β1-integrin-deficient cells

DNA methyltransferase (DNMT)-mediated promoter methylation can suppress *Ripk3* expression in cancer cell lines.[30] Although inhibition of DNMT activity by 5-Aza-2′-deoxycytidine (5′AZA) moderately increased *Ripk3* mRNA expression, this treatment did not normalize *Ripk3* mRNA levels in integrin-reconstituted cells (Figure S2A). Similarly, DNMT inhibition failed to restore *Ripk3* mRNA expression of β1-KO cells to the level of WT cells (Figure S2B). The CHD4/NuRD complex was recently shown to suppress RIPK3 in muscle stem cells and endothelial cells.[27,31] Notably, knockdown of CHD4 by three different short hairpin RNAs (shRNAs) significantly increased RIPK3 expression and fully normalized RIPK3 expression between WT and β1-KO cells, both at the protein level (Figures 2A and 2B) and at the mRNA level (Figure 2C). Moreover, live-cell imaging revealed that CHD4 depletion rendered necroptosis-resistant β1-KO cells hypersensitive to TNF-α/zVAD-induced necroptosis (Figure 2D). β1-WT and β1-KO cells showed comparable protein expression (Figure 2A) and nuclear localization (Figure S2C) of CHD4, suggesting that β1 integrin may regulate CHD4 activity rather than its expression or localization. We further tested whether CHD4-mediated RIPK3 repression is a conserved mechanism in other cell types. Transient knockdown of CHD4 by small interfering RNAs (siRNAs) significantly increased RIPK3 expression in β1-KO fibroblasts, B16-F10 melanoma cells, Panc02 pancreatic ductal adenocarcinoma (PDAC) cells, and MOVAS smooth muscle cells. However, cells with higher basal RIPK3 expression tended to be less responsive to CHD4 depletion in terms of RIPK3 upregulation. Notably, L929 cells expressed the highest levels of RIPK3 among the cell lines tested, at levels comparable to that in *Chd4* KO fibroblasts, which could not be further increased by CHD4 knockdown (Figures S2D and S2E).

The highly homologous class II CHDs including CHD3, CHD4, and CHD5 share a similar domain architecture and can all assemble NuRD and ChAHP complexes (Figure 2E). Whereas the nucleosome-remodeling activity resides in the central part of the protein, containing tandem plant homeodomain (PHD) and Chromo domains followed by an ATP-dependent helicase domain,[44] the assembly interface for NuRD and ChAHP resides in the C-terminal region. The less conserved N-terminal domain binds RNAs and plays a regulatory role.[40,49] To test whether other class II CHDs also regulate RIPK3 expression, EGFP control, hemagglutinin (HA)-tagged human CHD4 or CHD5, or a chimeric CHD4 containing the N-terminal regulatory domain of CHD5 ($CHD4^{CHD5\text{-}N}$) were stably expressed in β1 integrin KO

**Figure 1. β1 integrin links fibrotic signaling to RIPK3 expression in fibroblasts**

(A) pKO-αV, pKO-αV/β1, and pKO-β1 cells were seeded on fibronectin (FN)-coated coverslips for 24 h at confluence and treated with vehicle control, 50 ng/mL TNF-α, or 40 μM zVAD and 50 ng/mL TNF-α in combination for a further 8 h. Cells were stained with SytoxGreen (pseudocoloured in yellow) for 1 h before fixation with paraformaldehyde and immunostained for COL3 (magenta) and DAPI (cyan). Maximum intensity projection of z stack image series. Scale bar, 50 μm.

(B) Cells were seeded on FN-coated 24-well plates for 24 h at confluence and treated with vehicle control or 40 μM zVAD and 50 ng/mL TNF-α in combination in the presence of SytoxGreen. The time course of SytoxGreen signal intensity in time lapse movies is shown as a line graph of the mean ± SEM of three replicates.

(C) Cells were seeded on FN-coated 24-well plates for 24 h at confluence and treated with vehicle control or 40 μM zVAD and 50 ng/mL TNF-α in combination for 18 h. Normalized LDH release values are depicted as mean ± SD (n = 3); p value was calculated by two-way ANOVA with Tukey correction for multiple testing.

(D) Cells were treated as in (A), and protein expression of ITGB1, MLKL, and MLKL-pSer345 was analyzed by western blot. Vinculin (VCL) was used as loading control. Data are representative of 2 independent experiments.

(E) qPCR analysis of *Ripk3* transcript in pKO-αV, pKO-αV/β1, and pKO-β1 cells. Data were normalized to *Gapdh* and are depicted as mean ± SD (n = 3); p values were calculated on log-transformed data by one-way ANOVA with Tukey correction for multiple testing.

(F and G) Volcano plot comparison of DEseq2 count of RNA-seq data between pKO-αV and pKO-β1 cells (F) and between pKO-αV and pKO-αV/β1 cells (G).

(H) qPCR analysis of *Ripk3* transcript in β1-WT and β1-KO fibroblasts. Data were normalized to *Gapdh* and are depicted as mean ± SD (n = 3); p values were calculated on log-transformed data by an unpaired Student's t test.

(I) pKO-αV and β1-KO cells were reconstituted with mouse RIPK3 and treated as in (C), and LDH release was analyzed and is depicted as mean ± SD (n = 3); p values were calculated by two-way ANOVA with Šídák's correction for multiple testing (for every cell line, a comparison of unstimulated and stimulated cells was conducted).

(J) β1 integrin floxed fibroblasts were infected with adenovirus expressing Cre recombinase. Freshly sorted β1-KO cells were designated as passage 0 and passaged every 2 days. Protein expression of ITGB1 and RIPK3 of indicated passages was analyzed by western blot. GAPDH was used as a loading control. Data are representative of 2 independent experiments.

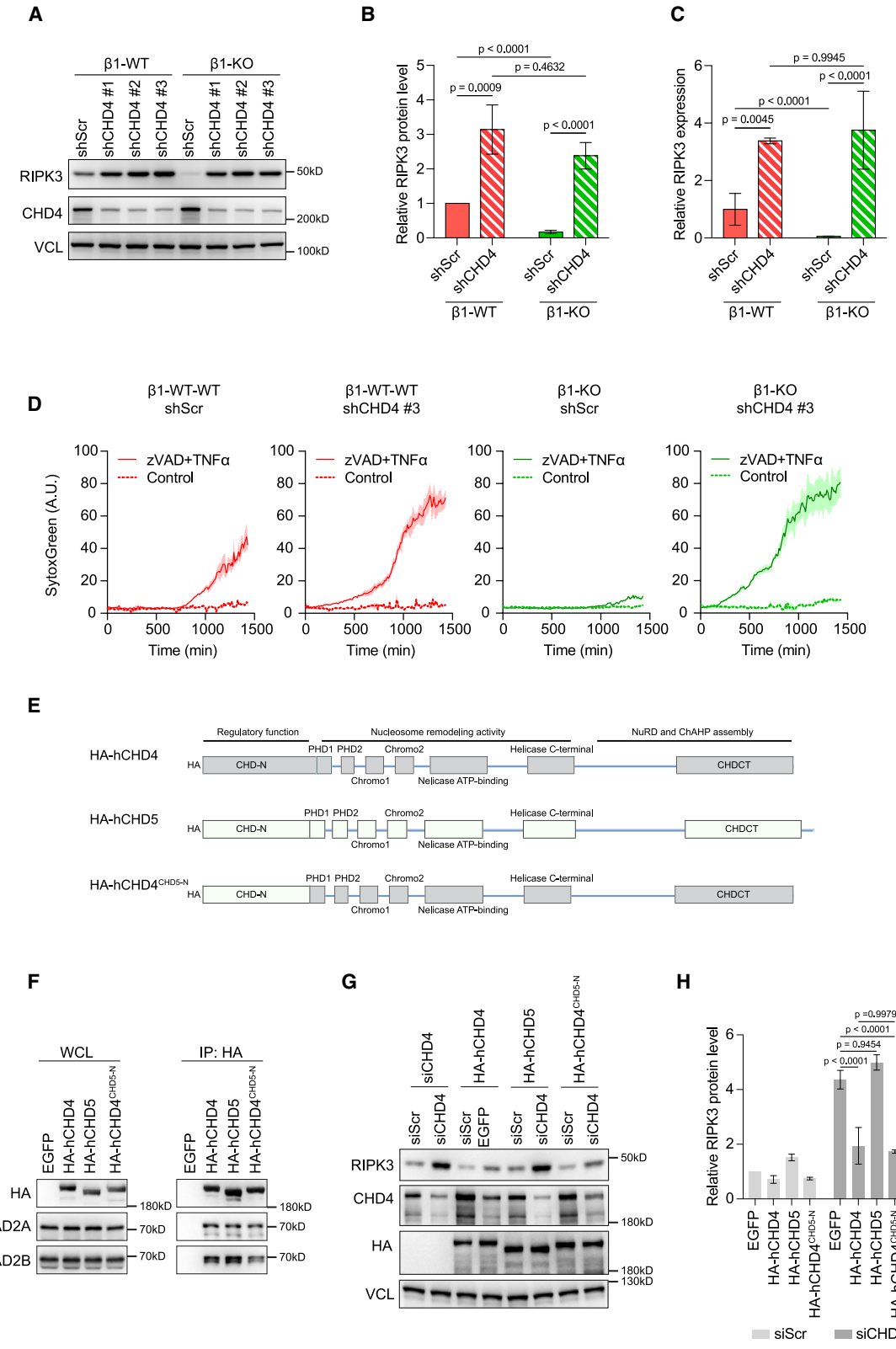


*(legend on next page)*

fibroblasts (Figure 2E). Immunoprecipitation of HA-tagged proteins confirmed that all CHD constructs were equally expressed and assembled into GATAD2A/B-containing NuRD complexes (Figure 2F). Interestingly, while transient knockdown of endogenous CHD4 by siRNAs targeting murine *Chd4* mRNA increased RIPK3 expression in cells expressing EGFP control and hCHD5, hCHD4 or hCHD4$^{CHD5\text{-}N}$ prevented RIPK3 upregulation upon knockdown of endogenous CHD4 (Figures 2G and 2H). Taken together, the loss of β1 integrin signaling results in CHD4-mediated repression of *Ripk3* transcription, a phenomenon well conserved across different cell types. Furthermore, CHD4 represses RIPK3 expression in a non-redundant manner within the class II CHD family proteins, and this function is conserved between mouse and human.

## CHD4 controls RIPK3 expression independent of the NuRD or ChAHP complex

The non-redundant function of CHD4 prompted us to test the involvement of NuRD and ChAHP. Recent biochemical analysis revealed that CHD4 is linked to the remainder of the NuRD complex through GATAD2A/B, with a possible contribution from CDK2AP1/2.[32,34] We therefore decoupled CHD4 from the NuRD complex by stable knockdown of GATAD2A/B and CDK2AP1/2 proteins (Figure 3A). Protein expression levels of all NuRD subunits were profiled by label-free quantification (LFQ) through mass spectrometry (Tables S4 and S5). For the ease of comparison, sums of LFQ intensity of paralogs are summarized in Figure 3B. CHD4 knockdown led to >80% reduction of CHD4 and CDK2AP1/2 proteins and approximately 50% reduction of other NuRD subunits including GATAD2A/B, MBD2/3, MTA1/2/3, and HDAC1/2. GATAD2A/B double knockdown resulted in >80% reduction of GATAD2A/B and CDK2AP1/2 proteins and approximately 50% reduction of other NuRD components including CHD3 and CHD4. CDK2AP1/2 knockdown predominantly affected the protein level of CHD3 (around 80% reduction), with only a mild effect on other NuRD subunits. Notably, ADNP levels were reduced by 50% upon CHD4 knockdown but remained intact upon GATAD2A/B or CDK2AP1/2 depletion. Paralog-specific effects were also documented (Figure S3A). For instance, CHD4 depletion preferentially reduced GATAD2A but not GATAD2B. MTA2, but not MTA1, was sensitive to GATAD2A/B or CHD4 depletion. Taken together, these data confirm mutual stabilization between NuRD subunits and independence between NuRD and ChAHP complexes. Moreover, depletion of the majority of CHD4 and GATAD2A/B by their respective shRNAs caused comparable disruption of the rest of the NuRD complex. Western blot of CHD4, GATAD2A, and GATAD2B confirmed the results of mass spectrometry (Figure 3C). Importantly, while CHD4 knockdown restored RIPK3 expression in β1 integrin KO cells, knockdown of GATAD2A/B or CDK2AP1/2 only slightly increased RIPK3 expression, likely due to the partial destabilization of CHD4 (Figure 3C).

To further confirm this result, we generated *Chd4* KO and *Gatad2a/b* double KO (DKO) in β1-KO cells. Consistently, *Chd4* KO or *Gatad2a/b* DKO led to a partial destabilization of the other (Figure 3D). Mass spectrometry analysis of the three *Chd4* KO clones confirmed the depletion of CHD4-derived peptides and the reduction of GATAD2A and GATAD2B proteins (Figure S3B). Immunoprecipitation of CHD4 revealed a robust association between CHD4 and HDAC1 but not with BRG1 or DNMT1 (Figure S3C). Of note, *Gatad2a/b* DKO completely disrupted this association and reduced HDAC1 coimmunoprecipitated with CHD4 to the background level of *Chd4* KO cells (Figure S3C). In contrast to the drastic upregulation of RIPK3 in *Chd4* KO clones, only a slight increase of RIPK3 could be observed in *Gatad2a/b* DKO clones (Figure 3D). While no basal cytotoxicity could be observed in *Chd4* KO or *Gatad2a/b* DKO cells in the LDH release assay, TNF-α/zVAD treatment triggered massive necroptosis only in *Chd4* KO cells (Figure S3D). Importantly, transient knockdown of CHD4 in *Gatad2a/b* DKO cells could strongly increase RIPK3 expression, with an effect size comparable to that of CHD4 knockdown in the parental β1-KO cells (Figure 3E). Finally, RIPK3 expression was not altered by 3 day treatment with the class I HDAC inhibitor TC-H 106 (Figure 3F). These data demonstrate that CHD4 suppresses RIPK3 expression independently of the NuRD complex or HDAC1/2 activity.

We next disrupted the ChAHP complex by stable knockdown of ADNP (Figure 3A). ADNP2 was not targeted since we did not detect its peptide in our cells by mass spectrometry (MS) analysis. ADNP knockdown resulted in 80% reduction of ADNP

**Figure 2. CHD4 represses RIPK3 expression in β1-integrin-deficient cells**

(A) β1-WT and β1-KO fibroblasts are transduced with lentivirus expressing scramble shRNA (shScr) or shRNAs targeting mouse CHD4 (shCHD4 #1,#2,#3). Protein expression of RIPK3 and CHD4 was analyzed by western blot. VCL was used as a loading control. Data are representative of 3 independent experiments.

(B) RIPK3 protein expression in (A) was quantified by densitometry and normalized to that in β1-WT expressing shScr and are depicted as mean ± SD (n = 3); p values were calculated on log-transformed data by a two-way ANOVA with Tukey correction for multiple testing.

(C) qPCR analysis of *Ripk3* transcript expression in β1-WT and β1-KO fibroblasts expressing shScr or CHD4 shRNA. Data are normalized to the mean value of the β1-WT/shScr controls and depicted as mean ± SD (n = 3); p values were calculated on log-transformed data by a two-way ANOVA with a Tukey correction for multiple testing.

(D) β1-WT and β1-KO fibroblasts expressing shScr or shCHD4 #3 were seeded on FN-coated 24-well plates for 24 h at confluence and treated with vehicle control or 40 μM zVAD and 50 ng/mL TNF-α in combination in the presence of SytoxGreen. Time lapse images were taken every 5 min for 24 h. The time course of SytoxGreen signal intensity is shown as a line graph of the mean ± SEM of three replicates.

(E) Domain architecture and functional annotation of human CHD4 and CHD5 and chimeric hCHD4$^{hCHD5\text{-}N}$.

(F) β1-KO fibroblasts were stably transduced by indicated constructs depicted in (E). HA-tagged CHD proteins were enriched by anti-HA beads, and coimmunoprecipitated GATAD2A and GATAD2B were analyzed by western blot. Data are representative of 2 independent experiments.

(G and H) Non-targeting control siRNA (siScr) or siRNA against mouse CHD4 (siCHD4) were transiently transfected for 72 h into the cell lines established in (F). Protein expression of CHD4 and HA-tagged CHDs as well as RIPK3 was analyzed by western blot using VCL as loading control (G). Data are representative of 3 independent experiments.

(H) Relative RIPK3 expression levels were quantified by densitometric analysis and are depicted as mean ± SD (n = 3); p values were calculated on log-transformed data by a two-way ANOVA with a Tukey correction for multiple testing.

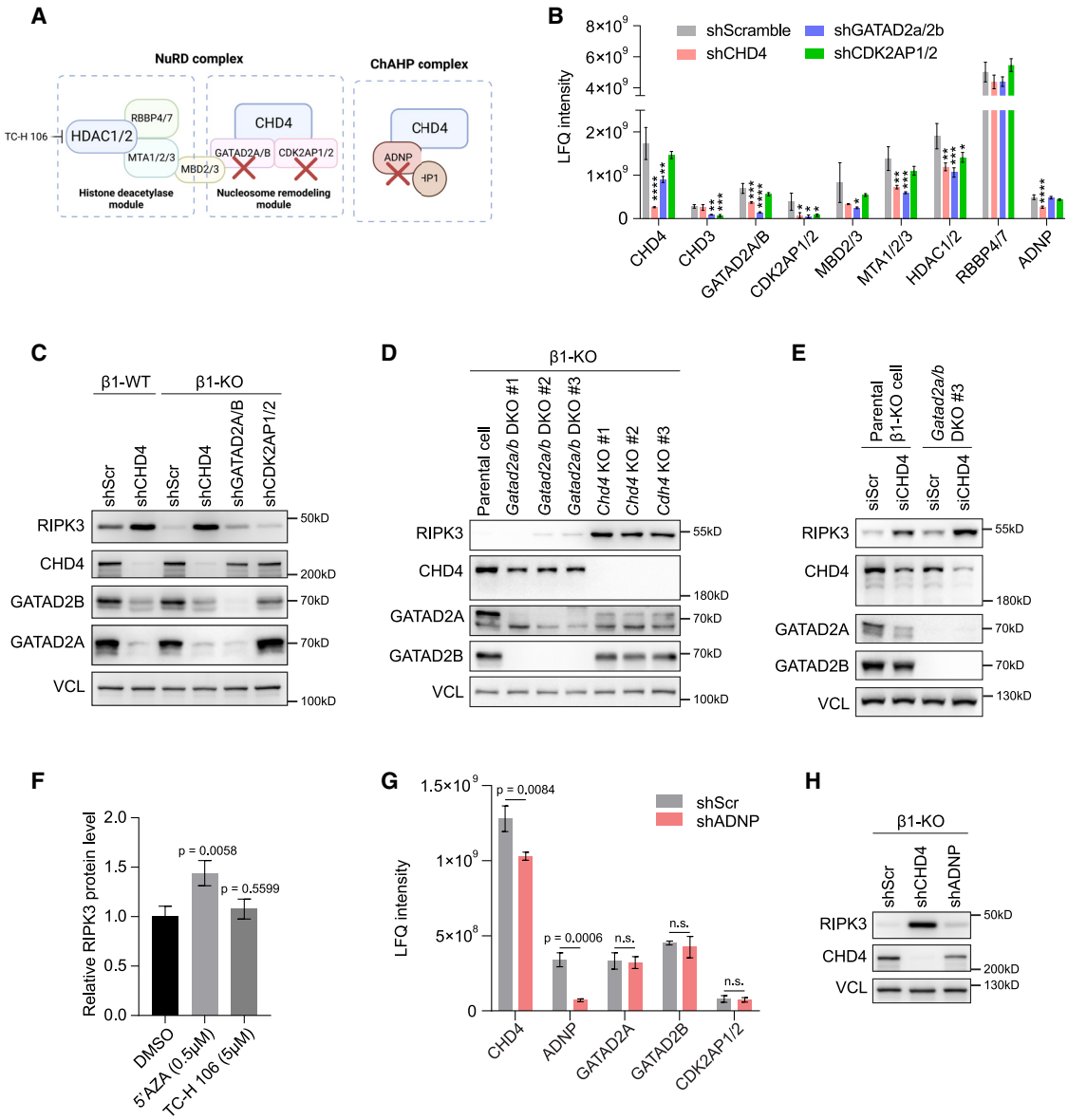


**Figure 3. CHD4 controls RIPK3 expression independently of the NuRD or ChAHP complex**

(A) Diagram of the modular assembly of the NuRD and ChAHP complexes. GATAD2A/B and CDK2AP1/2 were targeted to uncouple CHD4 from the rest of the NuRD complex; ADNP was targeted to disrupt the ChAHP complex. TC-H 106 was used to inhibit HDAC1/2 activity.

(B) Sum of LFQ intensity of paralogous subunits of NuRD and ChAHP in β1-KO cells stably expressing shScr or shRNAs targeting GATAD2A/B or CDK2AP1/2. Data are depicted as mean ± SD (n = 3); p values were calculated by one-way ANOVA with a Dunnett correction for multiple testing (for each protein or paralogous group, a comparison between the shRNA control and the other knockdown conditions was conducted). *p < 0.05; **p < 0.01; ***p < 0.001; ****p < 0.0001.

(C) Immunoblot of RIPK3, CHD4, GATAD2A, and GATAD2B using VCL as loading control in β1-WT and β1-KO cells expressing shScr or shRNA targeting CHD4, GATAD2A/B, or CDK2AP1/2. Data are representative of 2 independent experiments.

(D) Immunoblot of RIPK3, CHD4, GATAD2A, and GATAD2B in parental β1-KO cells, *Chd4* KO clones, and *Gatad2a/b* DKO clones using VCL as loading control. Data are representative of 2 independent experiments.

(E) Parental β1-KO cells and *Gatad2a/b* DKO cells were transiently transfected with non-targeting control siRNA or siRNA against mouse CHD4 for 72 h. Protein expression of CHD4, GATAD2A, GATAD2B, and RIPK3 was analyzed by immunoblot using VCL as a loading control.

(F) β1-KO cells were treated with DMSO control, 0.5 μM 5-Aza-2′-deoxycytidine (5′AZA), or 5 μM TC-H 106 for 72 h. RIPK3 protein level was analyzed by immunoblot and densitometry analysis. p values were calculated on log-transformed data by a one-way ANOVA with Dunnett correction for multiple testing for a comparison of the DMSO control with the other conditions.

(G) LFQ intensity of NuRD and ChAHP subunits in β1-KO cells stably expressing shScr or shRNA against ADNP. Data are presented as mean ± SD (n = 3); p values were calculated by a Student's t test.

(H) Immunoblot of RIPK3 or CHD4 using VCL as loading control in β1-KO cells expressing shScr or shRNA against CHD4 or ADNP.

protein and a mild reduction of CHD4 by 20% without affecting protein levels of other NuRD subunits (Figure 3G; Table 6). RIPK3, however, was only marginally increased in ADNP-depleted cells, likely due to the mild reduction of CHD4 (Figure 3H). In conclusion, our data indicated that CHD4-mediated suppression of RIPK3 expression is independent of the NuRD or the ChAHP complex.

## CHD4 exhibits high locus specificity independent of NuRD and ChAHP

Since CHD4 binds to the nucleosome and DNA without sequence preference, we investigated whether CHD4 could exhibit any locus specificity independent of the NuRD or the ChAHP complex. Whole-proteome comparison between β1 integrin KO cells expressing a scramble shRNA or a CHD4 shRNA revealed that the LFQ intensities of 1,113 proteins out of 6,498 quantified proteins were significantly altered (false discovery rate [FDR] < 0.05, S0 = 0.1; Tables S4 and S5). Besides RIPK3, a group of proteins related to the ECM, cytoskeleton, and metabolism were among the most significantly upregulated proteins in *CHD4* knockdown (KD) cells (Figure 4A). This included MCAM, BCAM, ALCAM, COL1A1, COL1A2, CNN1, CKB, GPD1, and ALPL. Importantly, whereas RIPK3 and CNN1 were too low to be quantified by MS in unperturbed cells (scramble shRNAs), their LFQ intensities increased to the upper 50$^{th}$ percentile in CHD4-depleted cells (Figure 4B). Thus, while CHD4 exerts genome-wide influence on gene expression, a group of genes including *Ripk3* exhibit an exceptional sensitivity to CHD4-mediated repression.

Whole-proteome analysis of CHD4-depleted cells, GATAD2A/B-depleted cells, and CDK2AP1/2-depleted cells revealed that 2,831 proteins among 6,498 quantified proteins were significantly changed in at least one of the cell lines (Figures 4C; Table S5). Notably, *Z* score clustering analysis revealed one group of 78 proteins strongly upregulated in CHD4-depleted cells but not in GATAD2A/B- or CDK2AP1/2-depleted cells and another group of 189 proteins preferentially upregulated in CHD4-depleted cells (Figure 4D). Surprisingly, the most significantly upregulated proteins in CHD4-depleted cells including RIPK3, CNN1, COL1A1, BCAM, ALPL, ALCAM, CKB, and GPD1 belong to these two clusters (Figures 4D and 4E). In contrast, none of these proteins were significantly upregulated in ADNP-depleted cells (Figure S4A; Table S6). qPCR analysis of a subset of CHD4-repressed genes in *Chd4* KO and *Gatad2a/b* DKO clones confirmed that the transcripts of *Cnn1*, *Ripk3*, *Bcam*, and *Alcam* were dramatically upregulated in *Chd4* KO cells (Figure 4F). *Cnn1* and *Bcam* were also slightly upregulated in *Gatad2a/b* DKO cells (Figure 4F), likely due to reduced CHD4 protein levels in these cells (Figure 3D). In contrast to the large changes in proteomics (Figure 4E), *Col1a1* transcripts showed only 2- to 3-fold upregulation in the three *Chd4* KO clones (Figure S4B). We took advantage of the collagen-binding-deficient β1-KO cells and analyzed protein expression of collagen type 1 by immunostaining. This experiment revealed a subpopulation (around 20%) of CHD4 KD cells with dramatic intracellular accumulation of collagen type 1 protein (Figure S4C). Hence, the increased collagen 1 protein levels in CHD4-deficient cells may be due to transcriptional upregulation in a subset of cells. In summary, CHD4 can potently suppress gene expression independent of the NuRD or ChAHP complex with exquisite locus specificity.

## Identification of CHD4-responsive CRE controlling RIPK3 expression

Previous chromatin immunoprecipitation (ChIP)-PCR studies have identified regions around the *Ripk3* locus that are enriched for binding of CHD4 and HDAC1.[27,31] However, our data showed that neither NuRD nor HDAC1/2 activity is required for CHD4-mediated RIPK3 repression. Moreover, widespread genome binding of NuRD and ChAHP complexes does not permit precise determination of CHD4-responsive CREs controlling RIPK3 expression. To resolve this issue, we performed assay for transposase-accessible chromatin using sequencing (ATAC-seq) experiments of the parental β1-KO cells, three individual *Chd4* KO clones, and three individual *Gatad2a/b* DKO clones. We further included β1-KO cells infected with a scramble shRNA virus to control random chromatin alteration due to genetic perturbation (ATAC-seq descriptive statistics in Table S7). Heatmap of *Z* score clustering (Figure 5A) and principal component analysis (PCA) (Figure S5A) revealed that control cells, *Chd4* KO clones, and *Gatad2a/b* DKO clones clustered into different groups with distinct chromatin-remodeling patterns. Among 74,164 retrieved ATAC-seq peaks, 17,284 were significantly increased and 7,969 were decreased in *Chd4* KO cells (Figures 5B; Tables S8 and S9). In contrast, *Gatad2a/b* DKO cells showed less effect on chromatin accessibility, with 5,012 ATAC peaks increased and 2,143 decreased (Figures 5C; Tables S10 and S11). Thus, both CHD4- and GATAD2A/B-containing NuRD complexes overall restrict chromatin accessibility. Approximately 4,000 increased and 1,600 decreased ATAC-seq peaks were found to be common for both *Chd4* KO and *Gatad2a/b* KO cells, which account for 73% significantly changed ATAC-seq peaks in *Gatad2a/b* DKO cells but only for 22% of those in *Chd4 KO* cells (Figure 5D). Moreover, for ATAC-seq peaks commonly changed in *Chd4* KO and *Gatad2a/b* DKO cells and for peaks uniquely changed in one of the KO cells, the effect size was significantly higher in *Chd4* KO cells (Figures 5E and 5F). Hence, although the majority of GATAD2A/B-dependent chromatin openings relied on CHD4, CHD4 exerts a much stronger and broader impact on chromatin accessibility independent of the NuRD complex.

We next functionally interrogated CHD4-responsive and GATAD2A/B-independent chromatin openings around the *Ripk3* locus using CRISPR silencing in *Chd4* KO cells stably expressing dCas9-KRAB-MeCP2.[50] Our ATAC-seq experiments had shown that there was no CHD4-responsive chromatin opening in regions previously identified by CHD4 ChIP-PCR around the *Ripk3* locus.[27,31] However, we observed a robust increase in chromatin accessibility around a distal enhancer and a proximal enhancer corresponding to EM10E0582741 and EM10E0582738 in ENCODE annotation, respectively (Figure 5G). Two single guide RNAs (sgRNAs) were stably expressed by lentiviral transduction to target the proximal (sgRipk3 enhP #1 and sgRipk3 enhP #2) and distal (sgRipk3 enhD #1 and sgRipk3 enhD #2) enhancers. To rule out the

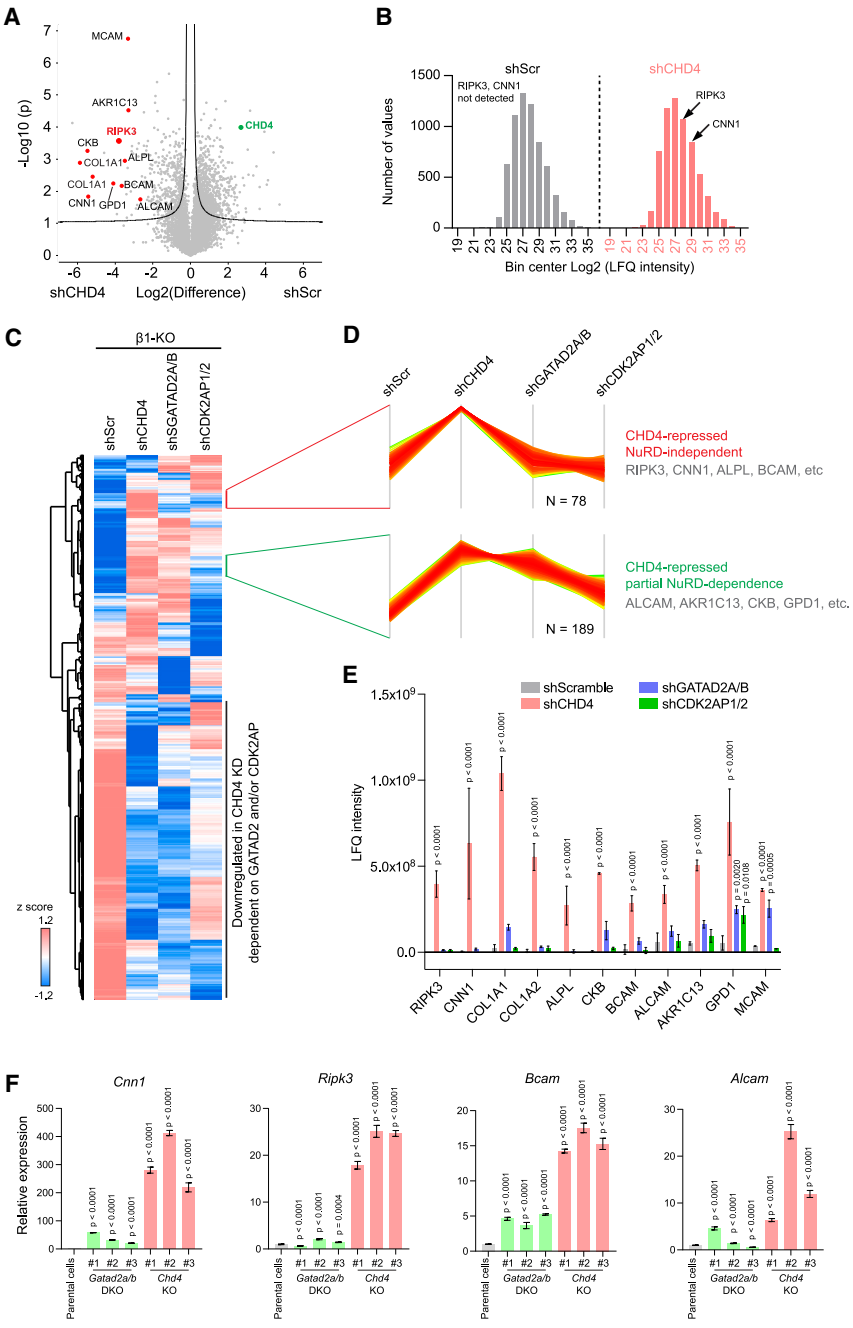


**Figure 4. CHD4 shows high locus specificity independent of NuRD and ChAHP complexes**

(A) Volcano plot of differential protein expression between β1-KO cells expressing shScr and CHD4 shRNA. CHD4 and outliers that were most significantly upregulated in CHD4-depleted cells, including RIPK3, are highlighted (n = 3; FDR = 0.05, S0 = 0.1).

(B) Histogram of log-transformed LFQ intensity distribution of the total proteome in indicated cells (bin width = 2). LFQ intensities of RIPK3 and CNN1 were too low to be quantified in shScr cells (left). Arrows indicate the positions of RIPK3 and CNN1 in CHD4-depleted cells (right).

(C) *Z* score heatmap of mean LFQ intensities of 2,833 differentially expressed proteins in control β1-KO, CHD4-depleted, GATAD2A/B-depleted, and CDK2AP1/2-depleted cells.

(D) A cluster of 78 proteins strongly upregulated in CHD4-depleted cells but not in GATAD2A/B- or CDK2AP1/2-depleted cells, including RIPK3, CNN1, ALPL, BCAM, etc., and another cluster of 189 proteins preferentially upregulated in CHD4-depleted cells, including ALCAM, AKR1C13, GPD1, CKB, etc., were identified.

(E) Untransformed LFQ intensities of the most significantly upregulated proteins in CHD4-depleted cells were compared between cell lines depleted of GATAD2A/B or CDK2AP1/2. Data are depicted as mean ± SD (n = 3); p values were calculated with a two-way ANOVA with Tukey correction for multiple testing (for each protein, a comparison between the shScr and the other knockdown conditions was conducted).

(F) qPCR analysis of *Cnn1*, *Ripk3*, *Bcam*, and *Alcam* transcript expression in parental β1-KO cells, *Chd4* KO clones, and *Gatad2a/b* DKO clones using *Gapdh* as normalization. Data are depicted as mean ± SD (n = 3); p values were calculated on log-transformed data by a one-way ANOVA with Tukey correction for multiple testing (for every cell line, a comparison with the parental cells was conducted).

non-specific effects of viral transduction and potential sgRNA off targets, we targeted the promoter and enhancer elements of the *Cnn1* locus, which had also gained accessibility in *Chd4* KO cells (sgCnn1 #1 and sgCnn1 #2; Figure 5H). While CRISPR silencing of the proximal enhancer of the *Ripk3* locus resulted in 95% reduction in *Ripk3* mRNA levels and markedly reduced RIPK3 protein levels, targeting the distal enhancer of the *Ripk3* locus had only a moderate influence (around 50% reduction) on *Ripk3* mRNA expression, with marginal statistical significance and no obvious reduction of RIPK3 protein expression (Figures 5I and S5C). Although none of the *Ripk3*-targeting sgRNAs affected *Cnn1* transcript expression, both *Cnn1*-targeting sgRNAs reduced the *Cnn1* transcript by 80%, with a minimal influence on *Ripk3* expression (Figures 5I and 5J). To test whether *Ripk3* expression is influenced by more distant CHD4-responsive elements via long-range genomic interactions, we also targeted other CHD4-responsive chromatin-opening regions within a 150 kb range around the *Ripk3* locus, most notably in nearby *Adcy4* and *Nfat3* loci (Figure S5B). However, none of these sgRNAs altered RIPK3 protein levels (Figure S5C). Finally, ChIP assays detected specific binding of CHD4 to the *Ripk3* proximal enhancer independent of GATAD2A/B (Figure 5K). Taken together, our results indicated that the CHD4-responsive proximal enhancer of the *Ripk3* locus is the primary driver of high *Ripk3* gene expression.

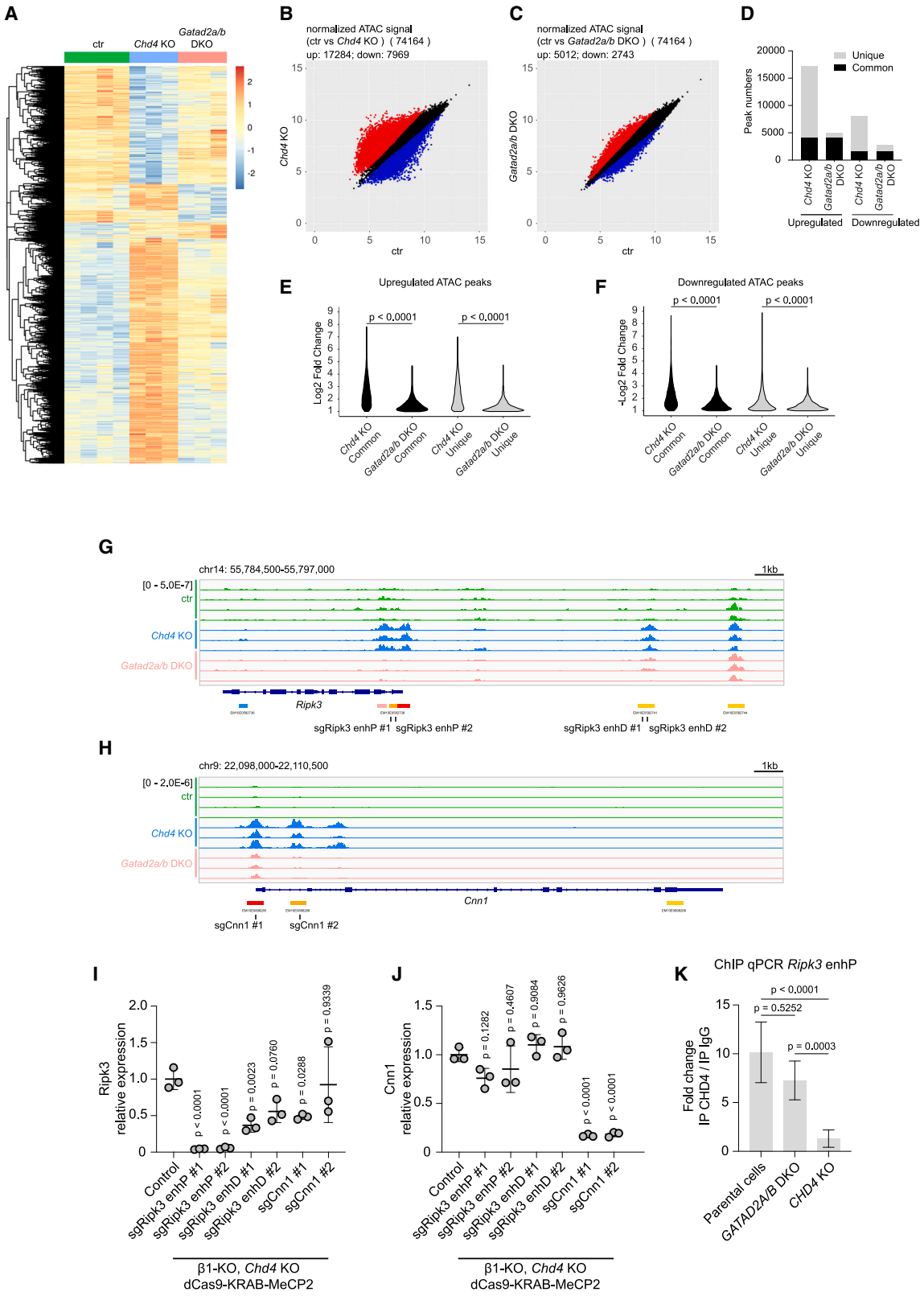


*(legend on next page)*

## DISCUSSION

Elevated RIPK3 expression is frequently observed in tissue fibrosis and may contribute to sustained TNF-α-driven inflammation in associated diseases.[23–27] By studying RIPK3 expression in BDL-induced liver fibrosis, we confirmed a strong increase of RIPK3 expression in fibrosing tissue, yet we made the unexpected finding of RIPK3 being primarily induced in myofibroblasts. This contrasts previous literature, where RIPK3 expression has mainly been attributed to the myeloid compartment. Hypothesizing that fibrotic signaling would be involved in this regulation, we targeted the β1 integrin receptor, which is required for collagen and fibronectin binding. Interestingly, loss of β1 integrin in fibroblasts not only abolished ECM fibrillogenesis but also led to repression of the *Ripk3* locus by the chromatin-remodeling factor CHD4. Surprisingly, this regulation displayed exquisite locus specificity and occurred independently of the NuRD or the ChAHP complex. Our data indicate that the β1 integrin receptor intrinsically links fibrotic signaling to RIPK3-driven inflammation via a novel mode of action of CHD4.

Precise transcriptional regulation requires concerted, locus-specific actions of transcription factors and epigenetic modifiers. Class II CHD proteins including CHD3, CHD4, and CHD5 are associated with two distinct chromatin-remodeling complexes, NuRD and ChAHP. Emerging evidence suggest that CHD4 may also function outside the NuRD complex. For instance, CHD4 only transiently associates with other preassembled NuRD subunits *in vitro* and processes nucleosome-remodeling activity by itself.[43] Mi-2β, the CHD4 homolog in Drosophila, suppresses germline gene expression in neurons independently of NuRD through a distinct complex containing Mep-1.[51] However, there is no Mep-1 homolog in vertebrates. Here, we provide definitive evidence that CHD4 can regulate gene expression independently of the NuRD or the ChAHP complex with supreme locus specificity and potency in mammalian cells. KO or KD of CHD4, GATAD2A/B, and ADNP uncoupled CHD4 from the NuRD or the ChAHP complex. Strikingly, the most significantly de-repressed genes in CHD4-depleted cells, which included *Ripk3*, *Cnn1*, *Bcam*, *Alcam*, etc., were not regulated by ChAHP or NuRD. Due to the interdependence of protein stability between subunits within the NuRD or the ChAHP complex,[52] depletion of GATAD2A/B resulted in an approximately 50% reduction of CHD4 protein level, which explains why some NuRD-independent CHD4 target genes are mildly perturbed by GATAD2A/B depletion.

ATAC-seq analysis revealed much stronger and broader alterations of chromatin accessibility in *Chd4* KO in comparison with *Gatad2a/b* DKO. Whereas the majority of chromatin openings in *Gatad2a/b* DKO cells are CHD4 dependent, 73% of CHD4-dependent chromatin openings do not depend on GATAD2A/B. Considering the 50% reduction of CHD4 in GATAD2A/B-depleted cells, the actual impact of the NuRD-independent function of CHD4 may be even larger. NuRD-independent functions of CHD4 may be contributed by the ChAHP complex. However, ADNP depletion caused only a 20% reduction of CHD4 (Figure 3G), suggesting that only a small portion of CHD4 is engaged in the ChAHP complex in our cells. Furthermore, it has been reported that only around 30% CHD4-dependent ATAC-seq loci overlap with ADNP-dependent loci.[53] Therefore, CHD4 has a profound impact on chromatin accessibility and gene expression independent of NuRD or ChAHP. Our observations thus call for caution in using CHD4/NuRD or CHD4/ChAHP as equivalent to CHD4.

CHD4 binds nucleosomes with no DNA sequence preference. Besides the high-affinity interactions with NuRD and ChAHP complexes, CHD4 may bind epigenetic marks and a plethora of transcription factors (TFs) to target to diverse genomic loci. Although class II CHDs can all assemble NuRD or ChAHP complexes, they non-redundantly regulate distinct genes in neurodevelopment *in vivo,*[38] which may be contributed by their unique "stand-alone" functions. For instance, we observed that *Ripk3* expression could be repressed by human CHD4 but not by human CHD5.

As one of the most prominent targets of the stand-alone function of CHD4, RIPK3 plays an essential role in TNF-α signaling and necroptosis. RIPK3 upregulation is reported in liver fibrosis.[24,28,29] However, despite the beneficial effect of RIPK3 inhibition in various liver disease models, it remains controversial whether RIPK3-mediated necroptosis is relevant in liver cell death due to its low expression in hepatocytes.[28,45] In BDL-induced liver fibrosis, we observed high RIPK3 expression in myofibroblasts and macrophages but not in hepatocytes. Since

**Figure 5. Identification of CHD4-responsive CRE controlling RIPK3 expression by ATAC-seq and CRISPR silencing**

(A) Heatmap clustering of differentially accessible regions (adjusted p value < 0.05 and log2 fold change > 1) between control, *Chd4* KO, and *Gatad2a/b* DKO cells.

(B and C) Scatterplot of differentially accessible regions between control cells and *Chd4* KO cells (B) and between control cells and *Gatad2a/b* DKO cells (C). Regions that gained or lost accessibility are highlighted in red or blue, respectively.

(D) ATAC-seq peaks that were commonly altered in both *Chd4* KO cells and *Gatad2a/b* DKO cells, or uniquely altered in only one cell line, were identified and counted.

(E and F) Violin plot showing the logarithmically transformed fold change of ATAC-seq signals of peaks commonly altered in both *Chd4* KO and *Gatad2a/b* DKO (E) or uniquely altered in one cell line (F). p values were calculated by Student's t test.

(G and H) ATAC-seq signal traces near the *Ripk3* locus (G) and *Cnn1* locus (H). ENCODE-annotated *cis*-regulatory elements are highlighted. The positions and names of individual CRISPR sgRNAs are annotated below with black lines.

(I and J) *Chd4* KO cells stably expressing dCas9-KRAB-MeCP2 were transduced with lentivirus expressing the indicated sgRNAs. mRNA expression of *Ripk3* (I) or *Cnn1* (J) in transduced cells and uninfected control cells was analyzed by qPCR. Data are depicted as mean ± SD (n = 3) normalized to the mean value of the control condition; p values were calculated on log-transformed data by a one-way ANOVA with Dunnett correction for multiple testing (a comparison of the control cells with all other cell lines was conducted).

(K) qPCR analysis of CHD4 binding at the *Ripk3* locus using a primer set detecting an amplicon within the *Ripk3* proximal enhancer region. Chromatin immunoprecipitation using a CHD4 antibody or immunoglobulin G (IgG) as control from parental cells, *Chd4* KO cells, and *Gatad2a/b* DKO cells. Data were normalized to the IgG control and are depicted as mean ± SD (n = 4); p values were calculated on log-transformed data by one-way ANOVA with Tukey correction for multiple testing.

myofibroblasts are the main culprits in driving excessive ECM deposition and tissue stiffening in fibrosis, we erased the fibrotic signature in *in-vitro*-cultured fibroblasts by genetic ablation of β1 integrin. This not only abolished ECM fibrillogenesis but also led to a progressive loss of RIPK3 expression. Conversely, reconstitution of β1 integrin in integrin pan-KO fibroblast cells drove high RIPK3 expression. Importantly, diminished RIPK3 expression in β1 integrin KO cells could be reverted by CHD4 depletion, suggesting that CHD4-mediated repression of the *Ripk3* locus is relieved in myofibroblasts downstream of β1 integrin signaling. We noticed upregulation of multiple fibrosis-related genes such as *Col1a1*, *Col1a2*, *Postn*, *Myh11*, etc., in muscle stem cells from *mdx* mice,[27] suggesting that the fibrotic signaling may be responsible for the attenuated suppression of *Ripk3* in DMD disease.

Integrin receptors can elicit pleiotropic signaling pathways depending on receptor subtypes. The unique signaling pattern of β1 integrin might be relayed to the *Ripk3* locus via a yet unknown CHD4-containing complex. Regulation of RIPK3 expression by β1 integrin signaling may be an integral part of the wound-healing response to provide general immune protection in structural cells.[54,55] However, it should be noted that integrin signaling is unlikely the only regulator of the *Ripk3* locus. The pivotal role of CHD4 at the *Ripk3* locus suggests that RIPK3 expression may be influenced by any perturbation of CHD4 activity. Considering the role of CHD4 in viral episome silencing,[40] the biological logic behind CHD4-mediated RIPK3 suppression might be rooted in antiviral immunity. Given the key functions of RIPK3 in inflammation and tumor immunology, targeting the standalone function of CHD4 may be a promising strategy to treat fibro-inflammation and to activate necroptosis in cancer cells. The set of CHD4-responsive genes defined in this study will allow genetic and chemical screening of novel CHD4 regulators in the future.

### Limitations of the study

Although our *in cellula* experiments point to an intrinsic connection between profibrotic β1 integrin signaling and RIPK3 expression, the contribution of β1 integrin signaling in RIPK3-dependent inflammation in various tissue fibrosis requires *in vivo* validation. Moreover, the signaling cascade connecting β1 integrin to CHD4 at the *Ripk3* locus remains largely unknown.

## STAR★METHODS

Detailed methods are provided in the online version of this paper and include the following:



## SUPPLEMENTAL INFORMATION

Supplemental information can be found online at https://doi.org/10.1016/j.celrep.2023.113322.

## ACKNOWLEDGMENTS

We thank Dr. Barbara Steigenberger (MPI Biochemistry) and the MS core facility of the Max Planck Institute of Biochemistry for MS proteomic analysis. We are grateful to Prof. Reinhard Fässler for generous support with critical cell models and research infrastructure in MPI Biochemistry. We thank Dr. Emanuel Rognoni and Dr. Michaela-Rosemarie Hermann for sample collection of RNA-seq analysis. We thank Dr. Mohammad Rahbari and Prof. Mathias Heikenwälder for insightful discussions and suggestions. This work is supported by the Deutsche Forschungsgemeinschaft (DFG, German Research Foundation) CRC 1403 (project number 414786233) and CRC 1335 (project number 360372040) to V.H. and TRR237 (project number 369799452) to V.H. and Z.A. Work in the G.S. lab is funded by the European Joint Programme on Rare Diseases (grant number EJPRD20-191).

## AUTHOR CONTRIBUTIONS

Z.S. and V.H. are responsible for the conceptualization of the study, data curation and analysis, and writing and editing of the manuscript. Z.S. performed most of the experiments. F.M.C. carried out the ATAC-seq experiments. F.M.C. and G.S. performed the ATAC-seq data analysis. H.H. and Z.A. provided mouse tissues samples of the BDL model. A.Y. performed RNA-seq analysis.

## DECLARATION OF INTERESTS

The authors declare no competing interests.

Received: May 4, 2023
Revised: August 29, 2023
Accepted: October 5, 2023
Published: October 25, 2023

## REFERENCES

1. Henderson, N.C., Rieder, F., and Wynn, T.A. (2020). Fibrosis: from mechanisms to medicines. Nature *587*, 555–566. https://doi.org/10.1038/s41586-020-2938-9.
2. Sun, Z., Costell, M., and Fässler, R. (2019). Integrin activation by talin, kindlin and mechanical forces. Nat. Cell Biol. *21*, 25–31. https://doi.org/10.1038/s41556-018-0234-9.
3. Sun, Z., Guo, S.S., and Fässler, R. (2016). Integrin-mediated mechanotransduction. J. Cell Biol. *215*, 445–456. https://doi.org/10.1083/jcb.201609037.

4. Schiller, H.B., Hermann, M.R., Polleux, J., Vignaud, T., Zanivan, S., Friedel, C.C., Sun, Z., Raducanu, A., Gottschalk, K.E., Théry, M., et al. (2013). beta1- and alphav-class integrins cooperate to regulate myosin II during rigidity sensing of fibronectin-based microenvironments. Nat. Cell Biol. *15*, 625–636. https://doi.org/10.1038/ncb2747.

5. Hermann, M.R., Jakobson, M., Colo, G.P., Rognoni, E., Jakobson, M., Kupatt, C., Posern, G., and Fässler, R. (2016). Integrins synergise to induce expression of the MRTF-A-SRF target gene ISG15 for promoting cancer cell invasion. J. Cell Sci. *129*, 1391–1403. https://doi.org/10.1242/jcs.177592.

6. Martin, K., Pritchett, J., Llewellyn, J., Mullan, A.F., Athwal, V.S., Dobie, R., Harvey, E., Zeef, L., Farrow, S., Streuli, C., et al. (2016). PAK proteins and YAP-1 signalling downstream of integrin beta-1 in myofibroblasts promote liver fibrosis. Nat. Commun. *7*, 12502. https://doi.org/10.1038/ncomms12502.

7. Danen, E.H.J., Sonneveld, P., Brakebusch, C., Fassler, R., and Sonnenberg, A. (2002). The fibronectin-binding integrins alpha5beta1 and alphavbeta3 differentially modulate RhoA-GTP loading, organization of cell matrix adhesions, and fibronectin fibrillogenesis. J. Cell Biol. *159*, 1071–1086. https://doi.org/10.1083/jcb.200205014.

8. van Loo, G., and Bertrand, M.J.M. (2023). Death by TNF: a road to inflammation. Nat. Rev. Immunol. *23*, 289–303. https://doi.org/10.1038/s41577-022-00792-3.

9. He, S., Wang, L., Miao, L., Wang, T., Du, F., Zhao, L., and Wang, X. (2009). Receptor interacting protein kinase-3 determines cellular necrotic response to TNF-alpha. Cell *137*, 1100–1111. https://doi.org/10.1016/j.cell.2009.05.021.

10. Cho, Y.S., Challa, S., Moquin, D., Genga, R., Ray, T.D., Guildford, M., and Chan, F.K.M. (2009). Phosphorylation-driven assembly of the RIP1-RIP3 complex regulates programmed necrosis and virus-induced inflammation. Cell *137*, 1112–1123. https://doi.org/10.1016/j.cell.2009.05.037.

11. Zhang, D.W., Shao, J., Lin, J., Zhang, N., Lu, B.J., Lin, S.C., Dong, M.Q., and Han, J. (2009). RIP3, an energy metabolism regulator that switches TNF-induced cell death from apoptosis to necrosis. Science *325*, 332–336. https://doi.org/10.1126/science.1172308.

12. Mompeán, M., Li, W., Li, J., Laage, S., Siemer, A.B., Bozkurt, G., Wu, H., and McDermott, A.E. (2018). The Structure of the Necrosome RIPK1-RIPK3 Core, a Human Hetero-Amyloid Signaling Complex. Cell *173*, 1244–1253.e10. https://doi.org/10.1016/j.cell.2018.03.032.

13. Sun, L., Wang, H., Wang, Z., He, S., Chen, S., Liao, D., Wang, L., Yan, J., Liu, W., Lei, X., and Wang, X. (2012). Mixed lineage kinase domain-like protein mediates necrosis signaling downstream of RIP3 kinase. Cell *148*, 213–227. https://doi.org/10.1016/j.cell.2011.11.031.

14. Murphy, J.M., Czabotar, P.E., Hildebrand, J.M., Lucet, I.S., Zhang, J.G., Alvarez-Diaz, S., Lewis, R., Lalaoui, N., Metcalf, D., Webb, A.I., et al. (2013). The pseudokinase MLKL mediates necroptosis via a molecular switch mechanism. Immunity *39*, 443–453. https://doi.org/10.1016/j.immuni.2013.06.018.

15. Rodriguez, D.A., Weinlich, R., Brown, S., Guy, C., Fitzgerald, P., Dillon, C.P., Oberst, A., Quarato, G., Low, J., Cripps, J.G., et al. (2016). Characterization of RIPK3-mediated phosphorylation of the activation loop of MLKL during necroptosis. Cell Death Differ. *23*, 76–88. https://doi.org/10.1038/cdd.2015.70.

16. Hildebrand, J.M., Tanzer, M.C., Lucet, I.S., Young, S.N., Spall, S.K., Sharma, P., Pierotti, C., Garnier, J.M., Dobson, R.C.J., Webb, A.I., et al. (2014). Activation of the pseudokinase MLKL unleashes the four-helix bundle domain to induce membrane localization and necroptotic cell death. Proc. Natl. Acad. Sci. USA *111*, 15072–15077. https://doi.org/10.1073/pnas.1408987111.

17. Pinci, F., Gaidt, M.M., Jung, C., Nagl, D., Kuut, G., and Hornung, V. (2022). Tumor necrosis factor is a necroptosis-associated alarmin. Front. Immunol. *13*, 1074440. https://doi.org/10.3389/fimmu.2022.1074440.

18. Cai, Z., Zhang, A., Choksi, S., Li, W., Li, T., Zhang, X.M., and Liu, Z.G. (2016). Activation of cell-surface proteases promotes necroptosis, inflammation and cell migration. Cell Res. *26*, 886–900. https://doi.org/10.1038/cr.2016.87.

19. Najjar, M., Saleh, D., Zelic, M., Nogusa, S., Shah, S., Tai, A., Finger, J.N., Polykratis, A., Gough, P.J., Bertin, J., et al. (2016). RIPK1 and RIPK3 Kinases Promote Cell-Death-Independent Inflammation by Toll-like Receptor 4. Immunity *45*, 46–59. https://doi.org/10.1016/j.immuni.2016.06.007.

20. Wong, W.W.L., Vince, J.E., Lalaoui, N., Lawlor, K.E., Chau, D., Bankovacki, A., Anderton, H., Metcalf, D., O'Reilly, L., Jost, P.J., et al. (2014). cIAPs and XIAP regulate myelopoiesis through cytokine production in an RIPK1- and RIPK3-dependent manner. Blood *123*, 2562–2572. https://doi.org/10.1182/blood-2013-06-510743.

21. Verjee, L.S., Verhoekx, J.S.N., Chan, J.K.K., Krausgruber, T., Nicolaidou, V., Izadi, D., Davidson, D., Feldmann, M., Midwood, K.S., and Nanchahal, J. (2013). Unraveling the signaling pathways promoting fibrosis in Dupuytren's disease reveals TNF as a therapeutic target. Proc. Natl. Acad. Sci. USA *110*, E928–E937. https://doi.org/10.1073/pnas.1301100110.

22. Wynn, T.A., and Ramalingam, T.R. (2012). Mechanisms of fibrosis: therapeutic translation for fibrotic disease. Nat. Med. *18*, 1028–1040. https://doi.org/10.1038/nm.2807.

23. Morgan, J.E., Prola, A., Mariot, V., Pini, V., Meng, J., Hourde, C., Dumonceaux, J., Conti, F., Relaix, F., Authier, F.J., et al. (2018). Necroptosis mediates myofibre death in dystrophin-deficient mice. Nat. Commun. *9*, 3655. https://doi.org/10.1038/s41467-018-06057-9.

24. Afonso, M.B., Rodrigues, P.M., Mateus-Pinheiro, M., Simão, A.L., Gaspar, M.M., Majdi, A., Arretxe, E., Alonso, C., Santos-Laso, A., Jimenez-Agüero, R., et al. (2021). RIPK3 acts as a lipid metabolism regulator contributing to inflammation and carcinogenesis in non-alcoholic fatty liver disease. Gut *70*, 2359–2372. https://doi.org/10.1136/gutjnl-2020-321767.

25. Takezaki, A., Tsukumo, S.I., Setoguchi, Y., Ledford, J.G., Goto, H., Hosomichi, K., Uehara, H., Nishioka, Y., and Yasutomo, K. (2019). A homozygous SFTPA1 mutation drives necroptosis of type II alveolar epithelial cells in patients with idiopathic pulmonary fibrosis. J. Exp. Med. *216*, 2724–2735. https://doi.org/10.1084/jem.20182351.

26. Imamura, M., Moon, J.S., Chung, K.P., Nakahira, K., Muthukumar, T., Shingarev, R., Ryter, S.W., Choi, A.M., and Choi, M.E. (2018). RIPK3 promotes kidney fibrosis via AKT-dependent ATP citrate lyase. JCI Insight *3*, e94979. https://doi.org/10.1172/jci.insight.94979.

27. Sreenivasan, K., Ianni, A., Künne, C., Strilic, B., Günther, S., Perdiguero, E., Krüger, M., Spuler, S., Offermanns, S., Gómez-Del Arco, P., et al. (2020). Attenuated Epigenetic Suppression of Muscle Stem Cell Necroptosis Is Required for Efficient Regeneration of Dystrophic Muscles. Cell Rep. *31*, 107652. https://doi.org/10.1016/j.celrep.2020.107652.

28. Preston, S.P., Stutz, M.D., Allison, C.C., Nachbur, U., Gouil, Q., Tran, B.M., Duvivier, V., Arandjelovic, P., Cooney, J.P., Mackiewicz, L., et al. (2022). Epigenetic Silencing of RIPK3 in Hepatocytes Prevents MLKL-mediated Necroptosis From Contributing to Liver Pathologies. Gastroenterology *163*, 1643–1657.e14. https://doi.org/10.1053/j.gastro.2022.08.040.

29. Gautheron, J., Vucur, M., Reisinger, F., Cardenas, D.V., Roderburg, C., Koppe, C., Kreggenwinkel, K., Schneider, A.T., Bartneck, M., Neumann, U.P., et al. (2014). A positive feedback loop between RIP3 and JNK controls non-alcoholic steatohepatitis. EMBO Mol. Med. *6*, 1062–1074. https://doi.org/10.15252/emmm.201403856.

30. Koo, G.B., Morgan, M.J., Lee, D.G., Kim, W.J., Yoon, J.H., Koo, J.S., Kim, S.I., Kim, S.J., Son, M.K., Hong, S.S., et al. (2015). Methylation-dependent loss of RIP3 expression in cancer represses programmed necrosis in response to chemotherapeutics. Cell Res. *25*, 707–725. https://doi.org/10.1038/cr.2015.56.

31. Colijn, S., Gao, S., Ingram, K.G., Menendez, M., Muthukumar, V., Silasi-Mansat, R., Chmielewska, J.J., Hinsdale, M., Lupu, F., and Griffin, C.T. (2020). The NuRD chromatin-remodeling complex enzyme CHD4 prevents hypoxia-induced endothelial Ripk3 transcription and murine embryonic vascular rupture. Cell Death Differ. *27*, 618–631. https://doi.org/10.1038/s41418-019-0376-8.

32. Low, J.K.K., Silva, A.P.G., Sharifi Tabar, M., Torrado, M., Webb, S.R., Parker, B.L., Sana, M., Smits, C., Schmidberger, J.W., Brillault, L., et al. (2020). The Nucleosome Remodeling and Deacetylase Complex Has an Asymmetric, Dynamic, and Modular Architecture. Cell Rep. *33*, 108450. https://doi.org/10.1016/j.celrep.2020.108450.

33. Ostapcuk, V., Mohn, F., Carl, S.H., Basters, A., Hess, D., Iesmantavicius, V., Lampersberger, L., Flemr, M., Pandey, A., Thomä, N.H., et al. (2018). Activity-dependent neuroprotective protein recruits HP1 and CHD4 to control lineage-specifying genes. Nature *557*, 739–743. https://doi.org/10.1038/s41586-018-0153-8.

34. Sharifi Tabar, M., Giardina, C., Feng, Y., Francis, H., Moghaddas Sani, H., Low, J.K.K., Mackay, J.P., Bailey, C.G., and Rasko, J.E.J. (2022). Unique protein interaction networks define the chromatin remodelling module of the NuRD complex. FEBS J. *289*, 199–214. https://doi.org/10.1111/febs.16112.

35. Sharifi Tabar, M., Mackay, J.P., and Low, J.K.K. (2019). The stoichiometry and interactome of the Nucleosome Remodeling and Deacetylase (NuRD) complex are conserved across multiple cell lines. FEBS J. *286*, 2043–2061. https://doi.org/10.1111/febs.14800.

36. Marques, J.G., Gryder, B.E., Pavlovic, B., Chung, Y., Ngo, Q.A., Frommelt, F., Gstaiger, M., Song, Y., Benischke, K., Laubscher, D., et al. (2020). NuRD subunit CHD4 regulates super-enhancer accessibility in rhabdomyosarcoma and represents a general tumor dependency. Elife *9*, e54993. https://doi.org/10.7554/eLife.54993.

37. Mor, N., Rais, Y., Sheban, D., Peles, S., Aguilera-Castrejon, A., Zviran, A., Elinger, D., Viukov, S., Geula, S., Krupalnik, V., et al. (2018). Neutralizing Gatad2a-Chd4-Mbd3/NuRD Complex Facilitates Deterministic Induction of Naive Pluripotency. Cell Stem Cell *23*, 412–425.e10. https://doi.org/10.1016/j.stem.2018.07.004.

38. Nitarska, J., Smith, J.G., Sherlock, W.T., Hillege, M.M.G., Nott, A., Barshop, W.D., Vashisht, A.A., Wohlschlegel, J.A., Mitter, R., and Riccio, A. (2016). A Functional Switch of NuRD Chromatin Remodeling Complex Subunits Regulates Mouse Cortical Development. Cell Rep. *17*, 1683–1698. https://doi.org/10.1016/j.celrep.2016.10.022.

39. Spruijt, C.G., Luijsterburg, M.S., Menafra, R., Lindeboom, R.G.H., Jansen, P.W.T.C., Edupuganti, R.R., Baltissen, M.P., Wiegant, W.W., Voelker-Albert, M.C., Matarese, F., et al. (2016). ZMYND8 Co-localizes with NuRD on Target Genes and Regulates Poly(ADP-Ribose)-Dependent Recruitment of GATAD2A/NuRD to Sites of DNA Damage. Cell Rep. *17*, 783–798. https://doi.org/10.1016/j.celrep.2016.09.037.

40. Kumar, A., Lyu, Y., Yanagihashi, Y., Chantarasrivong, C., Majerciak, V., Salemi, M., Wang, K.H., Inagaki, T., Chuang, F., Davis, R.R., et al. (2022). KSHV episome tethering sites on host chromosomes and regulation of latency-lytic switch by CHD4. Cell Rep. *39*, 110788. https://doi.org/10.1016/j.celrep.2022.110788.

41. Sher, F., Hossain, M., Seruggia, D., Schoonenberg, V.A.C., Yao, Q., Cifani, P., Dassama, L.M.K., Cole, M.A., Ren, C., Vinjamur, D.S., et al. (2019). Rational targeting of a NuRD subcomplex guided by comprehensive in situ mutagenesis. Nat. Genet. *51*, 1149–1159. https://doi.org/10.1038/s41588-019-0453-4.

42. Low, J.K.K., Webb, S.R., Silva, A.P.G., Saathoff, H., Ryan, D.P., Torrado, M., Brofelth, M., Parker, B.L., Shepherd, N.E., and Mackay, J.P. (2016). CHD4 Is a Peripheral Component of the Nucleosome Remodeling and Deacetylase Complex. J. Biol. Chem. *291*, 15853–15866. https://doi.org/10.1074/jbc.M115.707018.

43. Zhang, W., Aubert, A., Gomez de Segura, J.M., Karuppasamy, M., Basu, S., Murthy, A.S., Diamante, A., Drury, T.A., Balmer, J., Cramard, J., et al. (2016). The Nucleosome Remodeling and Deacetylase Complex NuRD Is Built from Preformed Catalytically Active Sub-modules. J. Mol. Biol. *428*, 2931–2942. https://doi.org/10.1016/j.jmb.2016.04.025.

44. Farnung, L., Ochmann, M., and Cramer, P. (2020). Nucleosome-CHD4 chromatin remodeler structure maps human disease mutations. Elife *9*, e56178. https://doi.org/10.7554/eLife.56178.

45. Kondylis, V., and Pasparakis, M. (2019). RIP Kinases in Liver Cell Death, Inflammation and Cancer. Trends Mol. Med. *25*, 47–63. https://doi.org/10.1016/j.molmed.2018.10.007.

46. Böttcher, R.T., Stremmel, C., Meves, A., Meyer, H., Widmaier, M., Tseng, H.Y., and Fässler, R. (2012). Sorting nexin 17 prevents lysosomal degradation of beta1 integrins by binding to the beta1-integrin tail. Nat. Cell Biol. *14*, 584–592. https://doi.org/10.1038/ncb2501.

47. Samson, A.L., Fitzgibbon, C., Patel, K.M., Hildebrand, J.M., Whitehead, L.W., Rimes, J.S., Jacobsen, A.V., Horne, C.R., Gavin, X.J., Young, S.N., et al. (2021). A toolbox for imaging RIPK1, RIPK3, and MLKL in mouse and human cells. Cell Death Differ. *28*, 2126–2144. https://doi.org/10.1038/s41418-021-00742-x.

48. Petrie, E.J., Sandow, J.J., Lehmann, W.I.L., Liang, L.Y., Coursier, D., Young, S.N., Kersten, W.J.A., Fitzgibbon, C., Samson, A.L., Jacobsen, A.V., et al. (2019). Viral MLKL Homologs Subvert Necroptotic Cell Death by Sequestering Cellular RIPK3. Cell Rep. *28*, 3309–3319.e5. https://doi.org/10.1016/j.celrep.2019.08.055.

49. Zhong, Y., Moghaddas Sani, H., Paudel, B.P., Low, J.K.K., Silva, A.P.G., Mueller, S., Deshpande, C., Panjikar, S., Reid, X.J., Bedward, M.J., et al. (2022). The role of auxiliary domains in modulating CHD4 activity suggests mechanistic commonality between enzyme families. Nat. Commun. *13*, 7524. https://doi.org/10.1038/s41467-022-35002-0.

50. Yeo, N.C., Chavez, A., Lance-Byrne, A., Chan, Y., Menn, D., Milanova, D., Kuo, C.C., Guo, X., Sharma, S., Tung, A., et al. (2018). An enhanced CRISPR repressor for targeted mammalian gene regulation. Nat. Methods *15*, 611–616. https://doi.org/10.1038/s41592-018-0048-5.

51. Aughey, G.N., Forsberg, E., Grimes, K., Zhang, S., and Southall, T.D. (2023). NuRD-independent Mi-2 activity represses ectopic gene expression during neuronal maturation. EMBO Rep. *24*, e55362. https://doi.org/10.15252/embr.202255362.

52. Burgold, T., Barber, M., Kloet, S., Cramard, J., Gharbi, S., Floyd, R., Kinoshita, M., Ralser, M., Vermeulen, M., Reynolds, N., et al. (2019). The Nucleosome Remodelling and Deacetylation complex suppresses transcriptional noise during lineage commitment. EMBO J. *38*, e100788. https://doi.org/10.15252/embj.2018100788.

53. Sun, X., Yu, W., Li, L., and Sun, Y. (2020). ADNP Controls Gene Expression Through Local Chromatin Architecture by Association With BRG1 and CHD4. Front. Cell Dev. Biol. *8*, 553. https://doi.org/10.3389/fcell.2020.00553.

54. Zhou, S., Zhang, W., Cai, G., Ding, Y., Wei, C., Li, S., Yang, Y., Qin, J., Liu, D., Zhang, H., et al. (2020). Myofiber necroptosis promotes muscle stem cell proliferation via releasing Tenascin-C during regeneration. Cell Res. *30*, 1063–1077. https://doi.org/10.1038/s41422-020-00393-6.

55. Krausgruber, T., Fortelny, N., Fife-Gernedl, V., Senekowitsch, M., Schuster, L.C., Lercher, A., Nemc, A., Schmidl, C., Rendeiro, A.F., Bergthaler, A., and Bock, C. (2020). Structural cells are key regulators of organ-specific immune responses. Nature *583*, 296–302. https://doi.org/10.1038/s41586-020-2424-4.

56. Yusa, K., Zhou, L., Li, M.A., Bradley, A., and Craig, N.L. (2011). A hyperactive piggyBac transposase for mammalian applications. Proc. Natl. Acad. Sci. USA *108*, 1531–1536. https://doi.org/10.1073/pnas.1008322108.

57. Ran, F.A., Hsu, P.D., Wright, J., Agarwala, V., Scott, D.A., and Zhang, F. (2013). Genome engineering using the CRISPR-Cas9 system. Nat. Protoc. *8*, 2281–2308. https://doi.org/10.1038/nprot.2013.143.

58. Pfeifer, A., Kessler, T., Silletti, S., Cheresh, D.A., and Verma, I.M. (2000). Suppression of angiogenesis by lentiviral delivery of PEX, a noncatalytic fragment of matrix metalloproteinase 2. Proc. Natl. Acad. Sci. USA *97*, 12227–12232. https://doi.org/10.1073/pnas.220399597.

59. Cox, J., and Mann, M. (2008). MaxQuant enables high peptide identification rates, individualized p.p.b.-range mass accuracies and proteome-wide protein quantification. Nat. Biotechnol. *26*, 1367–1372. https://doi.org/10.1038/nbt.1511.

60. Tyanova, S., Temu, T., Sinitcyn, P., Carlson, A., Hein, M.Y., Geiger, T., Mann, M., and Cox, J. (2016). The Perseus computational platform for comprehensive analysis of (prote)omics data. Nat. Methods *13*, 731–740. https://doi.org/10.1038/nmeth.3901.

61. Andrews, S. FastQC A Quality Control Tool for High Throughput Sequence Data.

62. Martin, M. (2011). Cutadapt removes adapter sequences from high-throughput sequencing reads. EMBnet. j. *17*, 10. https://doi.org/10.14806/ej.17.1.200.

63. Hannon, G.J. (2010). FASTX-toolkit: FASTQ/a Short-Reads Pre-processing Tools.

64. Illumina. iGenomes. https://support.illumina.com/sequencing/sequencing_software/igenome.html

65. Kim, D., Pertea, G., Trapnell, C., Pimentel, H., Kelley, R., and Salzberg, S.L. (2013). TopHat2: accurate alignment of transcriptomes in the presence of insertions, deletions and gene fusions. Genome Biol. *14*, R36. https://doi.org/10.1186/gb-2013-14-4-r36.

66. Liao, Y., Smyth, G.K., and Shi, W. (2014). featureCounts: an efficient general purpose program for assigning sequence reads to genomic features. Bioinformatics *30*, 923–930. https://doi.org/10.1093/bioinformatics/btt656.

67. Liao, Y., Smyth, G.K., and Shi, W. (2013). The Subread aligner: fast, accurate and scalable read mapping by seed-and-vote. Nucleic Acids Res. *41*, e108. https://doi.org/10.1093/nar/gkt214.

68. Anders, S., and Huber, W. (2010). Differential expression analysis for sequence count data. Genome Biol. *11*, R106. https://doi.org/10.1186/gb-2010-11-10-r106.

69. (2018). R: A Language and Environment for Statistical Computing (Vienna, Austria: R Foundation for Statistical Computing). (R Development Core Team).

70. Corces, M.R., Trevino, A.E., Hamilton, E.G., Greenside, P.G., Sinnott-Armstrong, N.A., Vesuna, S., Satpathy, A.T., Rubin, A.J., Montine, K.S., Wu, B., et al. (2017). An improved ATAC-seq protocol reduces background and enables interrogation of frozen tissues. Nat. Methods *14*, 959–962. https://doi.org/10.1038/nmeth.4396.

71. Cernilogar, F.M., Hasenöder, S., Wang, Z., Scheibner, K., Burtscher, I., Sterr, M., Smialowski, P., Groh, S., Evenroed, I.M., Gilfillan, G.D., et al. (2019). Pre-marked chromatin and transcription factor co-binding shape the pioneering activity of Foxa2. Nucleic Acids Res. *47*, 9069–9086. https://doi.org/10.1093/nar/gkz627.

72. Mezger, A., Klemm, S., Mann, I., Brower, K., Mir, A., Bostick, M., Farmer, A., Fordyce, P., Linnarsson, S., and Greenleaf, W. (2018). High-throughput chromatin accessibility profiling at single-cell resolution. Nat. Commun. *9*, 3647. https://doi.org/10.1038/s41467-018-05887-x.

73. Smith, J.P., Corces, M.R., Xu, J., Reuter, V.P., Chang, H.Y., and Sheffield, N.C. (2021). PEPATAC: an optimized pipeline for ATAC-seq data analysis with serial alignments. NAR Genom. Bioinform. *3*, lqab101. https://doi.org/10.1093/nargab/lqab101.

74. Jiang, H., Lei, R., Ding, S.W., and Zhu, S. (2014). Skewer: a fast and accurate adapter trimmer for next-generation sequencing paired-end reads. BMC Bioinf. *15*, 182. https://doi.org/10.1186/1471-2105-15-182.

75. Langmead, B., and Salzberg, S.L. (2012). Fast gapped-read alignment with Bowtie 2. Nat. Methods *9*, 357–359. https://doi.org/10.1038/nmeth.1923.

76. Faust, G.G., and Hall, I.M. (2014). SAMBLASTER: fast duplicate marking and structural variant read extraction. Bioinformatics *30*, 2503–2505. https://doi.org/10.1093/bioinformatics/btu314.

77. Robinson, J.T., Thorvaldsdóttir, H., Winckler, W., Guttman, M., Lander, E.S., Getz, G., and Mesirov, J.P. (2011). Integrative genomics viewer. Nat. Biotechnol. *29*, 24–26. https://doi.org/10.1038/nbt.1754.

78. Zhang, Y., Liu, T., Meyer, C.A., Eeckhoute, J., Johnson, D.S., Bernstein, B.E., Nusbaum, C., Myers, R.M., Brown, M., Li, W., and Liu, X.S. (2008). Model-based analysis of ChIP-Seq (MACS). Genome Biol. *9*, R137. https://doi.org/10.1186/gb-2008-9-9-r137.

79. Amemiya, H.M., Kundaje, A., and Boyle, A.P. (2019). The ENCODE Blacklist: Identification of Problematic Regions of the Genome. Sci. Rep. *9*, 9354. https://doi.org/10.1038/s41598-019-45839-z.

80. Love, M.I., Huber, W., and Anders, S. (2014). Moderated estimation of fold change and dispersion for RNA-seq data with DESeq2. Genome Biol. *15*, 550. https://doi.org/10.1186/s13059-014-0550-8.

81. Wickham, H. (2016). ggplot2 : Elegant Graphics for Data Analysis. Use R!, 2nd ed. (Springer International Publishing : Imprint: Springer).

82. Kolde, R. (2019). Pheatmap Pretty Heatmaps, 1.0.12 Edition.

## STAR★METHODS

### KEY RESOURCES TABLE

| REAGENT or RESOURCE | SOURCE | IDENTIFIER |
|---|---|---|
| **Antibodies** | | |
| Rat monoclonal anti β1 integrin | Chemicon | Clone MB1.2, MAB1997; RRID:AB_2128202 |
| Rabbit polyclonal anti Collagen-3 | Abcam | #ab7778; RRID:AB_306066 |
| Mouse polyclonal anti Collagen-1 | Chemicon | AB765P; RRID:AB_92259 |
| Rabbit monoclonal anti Phospho-mouse MLKL (Ser345) | Cell Signaling Technology | D6E3G, mAb #37333; RRID:AB_2799112 |
| Rabbit monoclonal anti mouse MLKL | Cell Signaling Technology | D6W1K, mAb #37705; AB_2799118 |
| Rabbit monoclonal anti mouse RIPK3 | Cell Signaling Technology | D4G2A, #95702; RRID:AB_2721823 |
| Rabbit polyclonal anti mouse RIPK3 | Abcam | ab62344; RRID:AB_956268 |
| Rat monoclonal anti mouse RIPK3 | Sigma-Aldrich | 8G7, MABC1595; RRID:AB_2940810 |
| Mouse monoclonal anti VCL | Sigma-Aldrich | V9131; RRID:AB_477629 |
| Mouse monoclonal anti VIMENTIN | Sigma-Aldrich | V5255; RRID:AB_477625 |
| Rat monoclonal anti mouse CD11b | PharMingen | 01711D; RRID:AB_393577 |
| Mouse monoclonal anti SMA, Cy3 conjugated | Sigma-Aldrich | C6198, clone 1A4; RRID:AB_476856 |
| Rabbit monoclonal anti CHD4 | Cell Signaling Technology | D4B7, #12011; RRID:AB_2734702 |
| Mouse monoclonal anti HA-tag | Santa Cruz Biotechnology | sc-7392, clone F-7; RRID:AB_627809 |
| Rabbit polyclonal anti GATAD2A | Sigma-Aldrich | HPA024373; RRID:AB_1849522 |
| Rabbit polyclonal anti GATAD2B | Sigma-Aldrich | HPA017015; RRID:AB_1854905 |
| Mouse monoclonal anti GAPDH | Calbiochem | CB1001, clone 6C5; RRID:AB_2107426 |
| Rabbit monoclonal anti BRG1 | Cell Signaling Technology | D1Q7F, mAb #49360; RRID:AB_2728743 |
| Rabbit polyclonal anti HDAC1 | Invitrogen | #PA1-860; PRID: AB_2118091 |
| Rabbit recombinant anti-DNMT1 [EPR18453] | Abcam | #ab188453; RRID:AB_2877711 |
| Goat polyclonal anti-mouse Alexa 488 | Invitrogen | A11029; RRID:AB_2534088 |
| Goat polyclonal anti-rabbit Alexa 488 | Invitrogen | A11008; RRID:AB_143165 |
| Goat polyclonal anti-mouse Alexa 546 | Invitrogen | A11010; RRID:AB_2534077 |
| Goat polyclonal anti-mouse Alexa 647 | Invitrogen | A21247; RRID:AB_141778 |
| **Chemicals, peptides, and recombinant proteins** | | |
| TC-H 106 | Selleckchem | Catalog No.S6738 |
| 5-Aza-2′-deoxycytidine | Santa Cruz Biotechnology | sc-202424 |
| Pan Caspase Inhibitor Z-VAD-FMK | R&D Systems | FMK001 |
| Recombinant TNF-α | PeproTech | 315-01A |
| SYTOX™ Green Nucleic Acid Stain | Invitrogen | S7020 |
| Lipofectamine 2000 | Invitrogen | #11668019 |
| **Critical commercial assays** | | |
| Invitrogen™ CyQUANT™ LDH Cytotoxicity Assay | Thermo Fisher Scientific | C20301 |
| iScript™ cDNA Synthesis Kit | Bio-Rad | #1708890 |
| SYBR® Green Supermix | Bio-Rad | #1708880 |
| SimpleChIP® Enzymatic Chromatin IP Kit | Cell Signaling Technology | #9003 |
| **Deposited data** | | |
| Raw MS data | This paper | PRIDE database: PXD041505 |

(*Continued on next page*)

*Continued*

| REAGENT or RESOURCE | SOURCE | IDENTIFIER |
|---|---|---|
| ATAC-seq data | This paper | GEO database: GSE229795 |
| Experimental models: Cell lines | | |
| β1-WT | R. T. Bottcher et al.[46] | N/A |
| β1-KO | R. T. Bottcher et al.[46] | N/A |
| pKO-αV | H. B. Schiller et al.[4] | N/A |
| pKO-αV/β1 | H. B. Schiller et al.[4] | N/A |
| pKO-β1 | H. B. Schiller et al.[4] | N/A |
| β1-KO *Chd4* KO clone #1, #2, #3 | This paper | N/A |
| β1-KO *Gatad2a/b* DKO clone #1, #2, #3 | This paper | N/A |
| L929 | ATCC | NCTC clone 929 |
| MOVAS | ATCC | CRL-2797 |
| MOVAS *Ripk3* KO | This paper | N/A |
| B16-F10 | ATCC | CRL-6475 |
| Panc02 | CLS | CVCL_D627 |
| Experimental models: Organisms/strains | | |
| Mouse: C57BL/6J | Janvier | N/A |
| Oligonucleotides | | |
| Primers for qPCR, see Table S2 | This paper | N/A |
| ON-TARGETplus Mouse Chd4 SMARTPool | Dharmacon | L-052142-00-0005 |
| Software and algorithms | | |
| ImageJ | | https://ImageJ.nih.gov/ij/index.html |
| Image Lab Software version 6.0 | Bio-Rad Laboratories | https://www.bio-rad.com/de-de/product/image-lab-software?ID=KRE6P5E8Z |
| GraphPad Prism version 9.0 | GraphPad Prism software | https://www.graphpad.com/ |

## RESOURCE AVAILABILITY

### Lead contact

Further information and requests for resources and reagents should be directed to and will be fulfilled by the lead contact, Veit Hornung (hornung@genzentrum.lmu.de).

### Materials availability

All newly generated materials associated with the paper are available upon request from the lead contact.

### Data and code availability

- The mass spectrometry proteomics data have been deposited to the ProteomeXchange Consortium via the PRIDE partner repository with the dataset identifier PRIDE: PXD041505. ATAC-seq data is deposited in the GEO database (https://www.ncbi.nlm.nih.gov/geo/) under accession number GSE229795. Source data and statistic test results for RNA-seq, proteomics and ATAC-seq are provided as Supplementary Tables. All other data that support the conclusions are available from the authors upon request.
- This paper does not report original code.
- Any additional information required to reanalyze the data reported in this work paper is available from the lead contact upon request.

## EXPERIMENTAL MODEL AND STUDY PARTICIPANT DETAILS

8–9-week-old mice of C57BL/6J (B6) background purchased from Janvier (Le Genest-Saint-Isle, France) were used for bile duct ligation. All mice were kept according to the guidelines of the Federation of Laboratory Animal Science Association and experiments were authorized by permission of the LANUV in the state of Northrhine Westfalia (AZ. 84–02.04.2017.A222).

## METHOD DETAILS

### Animals and bile duct ligation model

8-9 week old mice C57BL/6J (B6) were purchased from Janvier (Le Genest-Saint-Isle, France). Liver fibrosis was induced in male, 8–9 week old mice via bile duct ligation (BDL). Briefly, animals were treated with painkillers and anesthetized before the peritoneal cavity was opened along the linea alba. Two ligatures were placed around the common bile duct to obstruct it, before the incisions in the peritoneum and the skin were then closed, and the mice were allowed to recover. During the first 5 days after operation, all animals received additional injections of painkillers and liver injury was allowed to develop for 10 days before organs were harvested. Control mice were sham-operated (no ligation of the bile duct). All mice were kept according to the guidelines of the Federation of Laboratory Animal Science Association and experiments were authorized by permission of the LANUV in the state of Northrhine Westfalia (AZ. 84–02.04.2017.A222).

### Antibodies

Source of antibodies and their dilution for Western blot and immunostaining are listed in Table S1.

### Plasmids DNA

pBABE-mRIPK3 was acquired from Addgene (pBabe-puro-mRipk3, Addgene plasmid #78830). hCHD5 cDNA was purchased from Addgene (pENTR3c GW CHD5, Addgene plasmid #68869). hCHD4 cDNA was a gift from Lucas Farnung. cDNA encoding HA-tagged human CHD4 and CHD5 were amplified by PCR and inserted into pB-EF-Bos vector.[56] To generate chimeric protein of N terminus of hCHD5 fused to C terminus of hCHD4, DNA encoding a.a. 1-369 in hCHD4 was replaced by DNA encoding a.a. 1-342 in hCHD5. Stable knockdown was achieved by lentivirus. shRNAs were targeting mouse CHD4 (shCHD4 #1: 5′-GCCCATCTTCTGAGTTG TAAA-3’; shCHD4 #2: 5′-TCGAGTGAGGACGACGATTTA-3’; shCHD4 #3: 5′-CGTAAACAGGTCAACTACAAT-3′), GATAD2A (5′-GTGCTGCCAATAATGAGTTTA-3′), GATAD2B (5′-ACAGGAAATTGAACAGCGATT-3′), CDK2AP1 (5′-GAAAGAGATCAGACCGA CGTA-3′), CDK2AP2 (5′-TGGCAGAGACAGAACGCAATG-3′) and ADNP (5′-GCCTACAGATACCCTACTCAA-3′) were cloned into pLKO.1 vector. A scramble shRNA-expressing pLKO.1 (Addgene Plasmid #1864) was used as control (shScr). To generate knockout cells through CRISPR-Cas9, sgRNA targeting mouse *Chd4* (5′-TCTTACGGCTCCGACTACTG-3′), *Gatad2a* (5′-GGGCGCAC GAACCTGAAGTG-3′), *Gatad2b* (5′-CGTCTAGCACTCATATCCAC-3′) and *Ripk3* (5′-ACCCTCCCTGAAACGTGGAC-3′) were cloned into pSpCas9(BB)-2A-Puro (PX459) V2.0[57] (Addgene plasmid #62988). SgRNAs for CRISPR silencing (sgRipk3 enhP #1: 5′-GAAACCCGACGTCTACGGCT-3’; sgRipk3 enhP #2: 5′-TGTCTCCGGCACACCCACAC-3’; sgRipk3 enhD #1: 5′-ACGACAATCT GACACTTTGG-3’; sgRipk3 enhD #2: 5′-AGGAGACCTAAGTTGCTGCC-3’; sgCnn1 #1: 5′-GCCTGTCCCATTGGCCACGG-3’; sgCnn1 #2: 5′-GGCCCGCGCTATATAAGGGC-3’; sgAdcy4: 5′-GCGGGTACAGAAGTAAACCG-3’; sgNfat3 #1: 5′-GCGTGACAGT GATCTACAGT-3’; sgNfat3 #2: 5′-CTCCCGGTTTCAATCACCTG-3’; sgNfat3 #3: 5′-GTTTGTAAACGTCTGACCAG-3’; sgNfat3 #4: 5′-GTCGAAGGGTGATGCGTGCG-3’; sgNfat3 #5: 5′-GAAGCCATTTGCAAGAACCT-3’; sgNfat3 #6: 5′-GATGTCCCATGGGA TAAGGG-3’; sgNfat3 #7: 5′-CACTGGGGCTTTCAAATAGG-3’; sgNfat3 #8: 5′-CAGTGATAGCTGGGAATCAC-3′) were cloned into LentiSingle vector via ligation-independent cloning.

### Transient and stable gene expression in cell lines

SV40 large T-immortalized mouse kidney-derived fibroblasts have been previously described.[4,46] The cell lines used here were not found in the database of commonly misidentified cell lines maintained by ICLAC and NCBI BioSample. All cell lines were tested negative for mycoplasma contamination. All cell lines including MOVAS, L929, B16-F10, Panc02 were cultured in DMEM medium (Gibco) with 10% FBS (Gibco) and 1% penicillin–streptomycin (Gibco) under sterile conditions at 5% $CO_2$ and 95% humidity. All mouse kidney-derived fibroblasts were maintained on cell culture plates coated with 10 μg/ml fibronectin (FN, Calbiochem).

Transient transfections were carried out with Lipofectamine 2000 (Invitrogen) according to the manufacturer’s protocol. Briefly, 40 pmol ON-TARGETplus Mouse Chd4 SMARTPool siRNA (Dharmacon) was transfected with 4 μL Lipofectamine 2000 for each well of 6-well plate. 72 hours after transfection, cells lysates were collected for analysis.

To generate stable cell lines via lentivirus, VSV-G pseudo-typed lentiviral vectors were produced by transient transfection of HEK293T cells. Viral particles were concentrated from cell culture supernatant as previously described[58] and used for infection.

To generate cell line stably expressing N-terminally HA-tagged human CHD4, CHD5 and chimeric protein containing N terminus of hCHD5 fused to hCHD4 (HA-CHD4$^{CHD5-N}$), piggy bac plasmids encoding these proteins and plasmid encoding hyperactive piggy bac transposase were co-transfected into target cells and selected with 2 μg/mL puromycin for 1 week. For CRISPR silencing, *CHD4* KO cells was similarly transfected with piggy bac plasmid encoding dCas9-KRAB-MeCP2[50] (Addgene plasmid #110821) and selected with 10 μg/mL blasticidin for 1 week then infected with lentiviruses expressing different guide RNAs under U6 promoter.

To generate knockout cells through CRISPR-Cas9, 2 μg plasmid PX459 plasmid DNA was transfected with 4 μL Lipofectamine 2000 for each well of 6-well plate into indicated mouse kidney fibroblasts or MOVAS cells. 24 h after transfection, cells were selected with 2 μg/mL puromycin for 24–48 h. Surviving cells were single cell cloned into 96-well flat bottom plates at a density of 0.8 cell per well. Individual clones were expanded, and knockout was screened and validated by Western blot.

### Lactate dehydrogenase (LDH) release assay

LDH release was determined with CyQUANT LDH Cytotoxicity Assay kit (Thermo Fisher Scientific). 4x10$^5$ cells were seeded on FN-coated (10 μg/ml) 6-well plates overnight. Cells were treated either with control or with 40 μM zVAD and 50 ng/mL TNF-α for 18 h. Total cell lysates were generated by adding 10 x lysis buffer to cell culture at 37°C for 30 min. Total cell lysates and supernatants were cleared by centrifugation at 450*g* for 10 min. 20 μL of supernatants were mixed with 20 μL reaction reagent mix and incubated for 10–30 min at room temperature in the dark and measured on Tecan Spark20M microplate reader for absorbance at 490 nm and 680 nm. LDH activity is calculated by subtracting absorbance at 490 nm with absorbance at 680 nm. Cell culture media was used as blank control. Percentage of LDH release was calculated by dividing LDH activity in cell culture supernatant with LDH activity in whole cell lysate.

### Immunoprecipitation

For immunoprecipitation, 6x10$^5$ indicated cells were seeded overnight. Next day cells were briefly washed with PBS and lysed in IP buffer (50 mM TrisHCl, pH 7.4, 150 mM NaCl, 1% Triton X-100) supplemented with cOmplete, EDTA-free Protease Inhibitor Cocktail and Phosphatase Inhibitor Cocktail Set I and II (Sigma) at 4°C with mild sonication. Cell lysates were cleared by centrifugation at 15000*g* at 4°C for 20 min. Protein concentration of the supernatants of cell lysate were determined using BCA assay and normalized to 1 mg/mL with IP buffer and 0.5 mg protein input was used for each immunoprecipitation. When using *Chd4* KO and *Gatad2a/b* DKO clones, equal amounts of cell lysate from three clones were pooled to produce the input for immunoprecipitation. HA-tagged protein or CHD4 were immunoprecipitated with 2 μg anti-HA antibody (sc-7392, Santa Cruz) or 4 μL anti-CHD4 antibody (D4B7, Cell Signaling) with 20 μL slurry of Protein A/G PLUS-Agarose (Santa Cruz) at 4°C for 4 h with gentle mixing. Beads were washed three time with IP buffer and protein bound to the beads were eluted with Laemmli buffer supplemented with 10 mM TCEP at 95°C for 10 min. Elutes were separated in SDS–PAGE for Western blotting.

### SDS-PAGE and Western blot analysis

For protein analysis by Western blot, cells were lysed in RIPA buffer (50 mM TrisHCl, pH 7.4 at 4°C, 150 mM NaCl, 1% NP-40, 0.5% sodium deoxycholate, and 0.2% sodium dodecyl sulfate) supplemented with cOmplete, EDTA-free Protease Inhibitor Cocktail and Phosphatase Inhibitor Cocktail Set I and II (Sigma) at 4°C with brief sonication. Cell lysates were cleared by centrifugation at 15000*g* at 4°C for 20 min. Protein concentration of the supernatants were determined using BCA assay and normalized to 0.5 mg/mL with RIPA buffer and mixed with 4x Laemmli buffer supplemented with 10 mM TCEP. 5–10 μg protein samples were loaded for SDS-PAGE.

All SDS-PAGE were performed under reducing condition and transferred to PVDF membrane using tank transfer protocol. PVDF membranes were blocked with 5% BSA in PBST before incubating with primary antibodies overnight at 4°C. All Western blots were run in parallel or probed at different regions from the same PVDF membrane. No stripping or antibody re-probing was used in this study. Bio-Rad Image Lab Software was used for the densitometry analysis of images.

### Mass spectrometry proteomics

For sample preparation, lysed cell pellets (in 300 μL PreOmics Lyse buffer) were incubation at 95°C for 2 min and subsequently sonicated using a Bioruptor Plus sonication system (Diogenode) for 10 × 30 s at high intensity. Samples were incubated once more at 95°C for 2 min and sonicated. Then, samples were diluted 1:1 with water and digested for 1.5 h at 37°C with 1 μg of LysC and overnight at 37°C with 1 μg trypsin (Promega). The peptide mixture was acidified with trifluoroacetic acid (Merck) to a final concentration of 1%, followed by desalting of the peptides via SCX StageTips. Samples were vacuum dried and re-suspended in 6 μL of buffer A (0.1% formic acid).

For LC-MS/MS data acquisition, the peptides (3 μL) were loaded onto a 30 cm column (inner diameter: 75 μm; packed in-house with ReproSil-Pur C18-AQ 1.9-μm beads, Dr. Maisch GmbH) via the autosampler of the Thermo Easy-nLC 1200 (Thermo Fisher Scientific) at 60°C. Eluting peptides were directly sprayed onto the mass spectrometer Q Exactive HF (Thermo Fisher Scientific). Peptides were separated with a flow rate of 250 nL/min by a gradient of buffer B (80% ACN, 0.1% formic acid) from 2% to 30% buffer B over 120 min followed an increase to 60% B over 10 min then to 95% B over the next 5 min and finally the percentage of buffer B was maintained at 95% buffer B for another 5 min.

The mass spectrometer was operated in a data-dependent mode with MS1 scans from 300 to 1750 m/z (resolution of 60000 at m/z = 200), and up to 15 of the top precursors were selected for fragmentation using higher energy collisional dissociation (HCD with a normalized collision energy of value of 28). The MS2 spectra were recorded at a resolution of 15000 (at m/z = 200). AGC target for MS1 and MS2 scans were set to 3x10$^6$ and 1x10$^5$ respectively within a maximum injection time of 100 and 25 ms for MS1 and MS2 scans respectively.

For data analysis, raw data were processed using the MaxQuant computational platform[59] (version 1.6.17.0). Briefly, the peak list was searched against the Uniprot database of Mus musculus with an allowed precursor mass deviation of 4.5 ppm and an allowed fragment mass deviation of 20 ppm. MaxQuant by default enables individual peptide mass tolerances, which was used in the search. Cysteine carbamidomethylation was set as static modification, and methionine oxidation and N-terminal acetylation as variable modifications. The match-between-run option was enabled, and proteins were quantified across samples using the label-free quantification algorithm in MaxQuant generating label-free quantification (LFQ) intensities.

Statistical analysis of MS measurements was performed in Perseus.[60] Briefly, raw data was filtered for proteins only identified by site, reverse peptide, and contaminants. Logarithmic transformation of LFQ intensities were filtered for valid values in 3 replicates in at least one cell types with imputation of missing values using default setting in Perseus (width = 0.3, down shift = 1.8). Volcano plot for comparison between two samples was calculated using standard student t-test (FDR = 0.05, S0 = 0.1). One-way ANOVA was used for statistical analysis of multiple comparison based on logarithmically transformed data (permutation-base FDR of 0.05). Significant targets were filtered, and *Z* score was calculated based on the mean value of their logarithmically transformed LFQ intensities. Original untransformed LFQ intensities were plotted in bar graphs.

### Quantitative RT-qPCR

RNA was extract from indicated cells using TRIzol reagent. Extracted RNAs were diluted into 100 ng/μL concentration. 500 ng total RNA was used for cDNA synthesis using iScript cDNA Synthesis Kit (Bio-Rad). cDNA synthesized from 5ng total RNA was used as template for qPCR with SYBR Green mater mix (Bio-Rad) using a PCR setting of 95°C, 3 min; 95°C, 30 s; 58°C, 20 s; 72°C, 15 s for 45 cycles. All qPCR primers were designed by Integrated DNA Technologies IDT with Tm value between 57°C and 59°C and are listed in Table S2.

### Chromatin IP-qPCR analysis

Chromatin-IP (ChIP) was conducted using SimpleChIP Enzymatic Chromatin IP Kit with magnetic beads (Cell Signaling #9003). Briefly, for each cell line, $5x10^6$ cells cultured on 15 cm cell culture plate were crosslinked with 1% fresh glutaraldehyde at room temperature for 10 min. The crosslinking reaction was quenched by glycine. Cell nuclei was fractionated, and chromatin DNA digestion was conducted in 400 μL resuspended nuclear fraction with 1 μL micrococcal nuclease supplied in the kit for 20 min at 37°C and stopped by 50 mM EDTA. For *Chd4* KO and *Gatad2a/b* DKO, nuclear fraction of equal amounts of cells were pooled before nuclease digestion. Nuclei was then sonicated in 500 μL ChIP Buffer and clarified by centrifugation at 9500*g* in a microcentrifuge for 10 min at 4°C. 200 μL digested chromatin preparation was incubated with 2 μL ChIP grade CHD4 antibody (D4B7, Cell Signaling #12011) or IgG control supplied in the kit for 10 h at 4°C with constant rotation and subsequently with 25 μL protein G magnetic beads for another 2 h at 4°C. The bound chromatin fragments were eluted, and the crosslinks were reversed by proteinase K digestion. The released chromatin DNA was further purified into 40 μL elute with DNA purification spin columns supplied in the kit. 4 μL DNA elute was used for qPCR analysis using a primer set (forward: 5′-CTTTGTCAAGCTCATTTCCTGG-3'; reverse: 5′-TCTTGCTCAGTGTCCTTGC-3′) amplifying within the proximal enhancer region in *Ripk3* locus.

### RNA-seq data analysis

After checking the quality of the samples (FastQC, v.0.10.1),[61] cutadapt (v.1.4.1)[62] was used to remove the adapters and all reads which are afterward were shorter than 80 bp, followed by fastx_trimmer[63] (fastx toolkit, v. 0.0.14) to remove the first 10 nt from the beginning of the reads (-f 11 -L 151 -Q33). When reads quality was assured, the files were mapped to the mouse genome (Genome build *NCBIM37*) downloaded from the iGenomes[64] using the tophat aligner (v. 2.0.11)[65] with default parameters for both single- and paired-end samples in the dataset. The mapped files were then quantified on a gene level based on the ensembl annotations, using the featureCounts[66] (v. 1.4.2) tool from the SubRead package[67] (v. 2.0.1). Using the DESeq2[68] package (R 3.0.3,[69] DESeq2 version 1.2.10) the count data was normalized by the size factor to estimate the effective library size. This followed by the calculation of gene dispersion across all samples.

Perseus was used to perform statistical analysis of the RNA count data. Briefly, normalized DESeq2 count data was logarithmically transformed and filtered for valid values found in 3 replicates in at least one cell types with imputation of missing values using default setting in Perseus (width = 0.3, down shift = 1.8). Volcano plot for comparison between two samples was calculated using standard student t-test (FDR = 0.05, S0 = 1).

### ATAC-seq library preparation and data analysis

Omni-ATAC was performed as previously described[70] with minor modifications.[71] Briefly, 50000 cells were washed in 1x PBS, resuspended in 50 μL of ATAC-seq resuspension buffer (RSB: 10 mM Tris-HCl, pH 7.4, 10 mM NaCl, and 3 mM $MgCl_2$) containing 0.1% NP40, 0.1% Tween 20 and 0.01% digitonin (Promega) and were incubated on ice for 3 min. Following lysis, 1 mL of ATAC-seq RSB containing 0.1% Tween 20 was added, and nuclei were centrifuged at 500*g* (4°C, 10 min). Pelleted nuclei were resuspended in 50 μL of transposition mix (25 μL 2 × TD buffer, 2.5 μL Tagment DNA enzyme (Illumina Tag DNA Enzyme and Buffer Kit, cat. 20034197), 16.5 μL PBS, 0.5 μL 1% digitonin, 0.5 μL 10% Tween 20, and 5.25 μL water) and incubated at 37°C for 30 min in a thermomixer shaking at 1000 rpm. DNA was purified using Qiagen PCR clean-up MinElute kit (Qiagen). The transposed DNA was subsequently amplified in 50 μL reactions with custom primers as described.[72] After 4 cycles libraries were then monitored with qPCR: 5 μL PCR sample in a 15 μL reaction with the same primers. qPCR output was monitored for the ΔRN; 0.25 ΔRN cycle number was used to estimate the number of additional cycles of the PCR reaction needed for the remaining PCR samples. Amplified libraries were purified with the Qiagen PCR clean-up MinElute kit (Qiagen) and size selected for fragments shorter than 600 bp using the Agencourt AMPure XP beads (Beckman Coulter). Libraries were quality controlled by Qubit and Agilent DNA TapeStation analysis. Paired-end sequencing (60 bp) was performed on an Illumina Next-Seq 2000 instrument.

The PEPATAC pipeline[73] (version 0.10.3) with default settings was used for primary analysis and quality controls. Briefly, after adapter trimming with Skewer[74] reads were first pre-aligned with bowtie2[75] to the mouse_chrM2x mitochondrial genome (parameters: -k 1 -D 20 -R 3 -N 1 -L 20 -i S,1,0.50) to remove mitochondrial reads and then mapped to the mm10 mouse genome (parameters: –very-sensitive -X 2000). Following alignment, reads with mapping quality scores below 10 and any residual mitochondrial reads were removed and read deduplication was carried out using Samblaster.[76] Alignments were used to generate a signal track for visualization with IGV genome browser.[77] MACS2[78] was used for peak-calling (parameters: –shift −75 –extsize 150 –nomodel –call-summits –nolambda –keep-dup all -p 0.01). Called peaks were filtered against the ENCODE blacklist[79] and were standardized by extending up and down 250 bases from the summit of each peak to establish peaks 500 bases in width.

To establish consensus peaks, overlapping (1 bp) peaks between every sample in the project were identified and the consensus peak's coordinates based on the overlapping peak with the highest score were defined. Peaks present in at least 2 samples with a minimum score per million $\geq 5$ were retained. A peak count table was then provided where every sample peak set is overlapped against the consensus peak set. Individual peak counts for an overlapping peak were weighted by multiplying by the percent overlap of the sample peak with the consensus peak. The consensus peak counts table was loaded into R[69] (version 4.1.0) and DESeq2[80] (version 1.32.0) was used for normalization and identification of significant differential accessible regions (adjusted p value <0.05 and log2 fold change >1). ggplot2[81] (version 3.3.5) and pheatmap[82] (version 1.0.12) were used data visualization. Samples mapping statistics and quality controls summary are provided in Table S7.

### Immunofluorescence microscopy

For immunofluorescence of fixed cells, cells cultured on FN-coated (10 μg/mL) coverslips were fixed with 4% PFA at room temperature for 20 min before staining. For immunostaining of extracellular collagen type 3, cells were washed twice with PBS, blocked with 5% BSA in PBS for 1 h and directly incubated with the primary antibody diluted in PBS at 4°C overnight. For immunostaining of intracellular proteins, fixed cells were permeabilized with 0.1% Triton X-100 in PBS for 20 min at room temperature. For immunostaining of tissue samples, 7 μm thick cryosections were permeabilized with 0.05% Triton X-100 in PBS for 30 min at room temperature. Permeabilized samples were blocked with 5% BSA in PBS for 1 h at room temperature followed by incubation with the primary antibodies in 3% BSA in PBS overnight at 4°C and then with fluorescently conjugated secondary antibodies for 1 h at room temperature. DNA was briefly stained with DAPI for 5 min at room temperature. Images were collected at room temperature on a Zeiss (Jena) LSM780 confocal laser scanning microscope equipped with a Zeiss Plan-APO 63x–numerical aperture 1.46 oil immersion objective. Images were processed by ImageJ.

### Live cell imaging

$3x10^5$ indicated cells were seeded on FN-coated (10 μg/mL) plates overnight. Cells were treated with vehicle control, 40 μM zVAD, 50 ng/mL TNF-α and 40 μM zVAD in combination as indicated in the presence of 5 μM SytoxGreen (S7020, Invitrogen) and transferred to EVOS FL Auto live cell imaging system (Thermo Fisher Scientific) with environment control at 37°C and 5% $CO_2$. Temperature and focus were stabilized for 30 min before brightfield, and epifluorescence images were taken with 20x objective every 5 min for 24 h. Fluorescent signals in time series images were measured by ImageJ.

## QUANTIFICATION AND STATISTICAL ANALYSIS

Statistical analysis was carried out in GraphPad Prism software (version 9.00, GraphPad Software). Statistical calculations to predetermine required sample size were not carried out. Datasets were analyzed using either Student's t-tests, one-way ANOVA, or two-way ANOVA with additional corrections for multiple testing as indicated. In some graphs only the p values of relevant comparisons are shown. Results are depicted as mean ± s.d. or mean ± s.e.m. as indicated in figure legends. All experiments for quantitative analysis were reproduced at least three times.